Science Advances
AAAS

Supplementary Materials for

The rise of lichens during the colonization of terrestrial environments

Bruno Becker-Kerber *et al.*

Corresponding author: Bruno Becker-Kerber, bkerber@fas.harvard.edu

Sci. Adv. **11**, eadw7879 (2025)
DOI: 10.1126/sciadv.adw7879

The PDF file includes:

Supplementary Text
Figs. S1 to S14
Table S1
Legend for data S1
References

Other Supplementary Material for this manuscript includes the following:

Data S1

Supplementary Text

Fossil provenance

The sample containing the connected thallus elements of *Spongiophyton* was collected by B.B.K. and G.K. in 2021. The fossils were found in a quarry in Rio Verde de Mato Grosso city, Mato Grosso do Sul State, Brazil, at the coordinates: 18°56'26.51"S–54°50'16.92"W. The fossils were identified and validated by B.B.K. and the Pragian-Emsian age of the rocks was determined based on the well-known biostratigraphy reported in previous works (see section 'Geology and age'). The sample containing the numerous thalli of *Spongiophyton* is deposited in the geological and paleontological collection of the Brazilian Synchrotron Light Laboratory (LNLS) under the acronym CNPEM-001.

Geology and age

The fossiliferous horizon occurs towards the middle of the section and its lithology is mostly composed of shale and silty shale, with rare thin intercalations of siltstone and sandstone layers (fig. S9). However, upsection there is a coarsening-upward trend, and the fine-grained mudstones and siltstones are capped by deltaic sandstones, a common trend in the Devonian sections of Mato Grosso do Sul State (*85*, *86*). These Early Devonian successions belong to the Ponta Grossa Formation (Alto Garças Sub-Basin), also previously referred to as Lower Unit 2 (*87*), and are correlated with the well-known deposits of the Ponta Grossa Formation in the Apucarana Sub-Basin, Paraná Basin, southern Brazil.

The Pragian-Early Emsian age of the Ponta Grossa Formation (Lower Unit 2) deposits nearby Rio Verde de Mato Grosso is well established based on palynological works (*88*). However, at the locality of the fossils studied here, formerly referred as "Felix" Quarry, the fine-grained siliciclastic facies initially only yielded Pragian age palynomorphs (i.e., *Ramochitina magnifica*), while no Emsian chitinozoan was observed (*89*). More recently, Sedorko et al. (*90*) considered a late Pragian-early Emsian age for these rocks. Therefore, we follow these works and regard the strata yielding *Spongiophyton* as Pragian-Emsian in age (ca. 410 Ma).

Taxonomy

Family Spongiophytaceae Kräusel and Venkatachala, 1966 (*91*)
Genus *Spongiophyton* Kräusel emend. Chaloner et al., 1974 (*43*)
Type species. *Spongiophyton lenticulare* (Barbosa) Kräusel (*12*) emend Chaloner et al., 1974 (*43*)

Spongiophyton nanum Kräusel emend. Chaloner et al., 1974

Figs. 1-3; fig. S1

Description. Flattened and dorsiventrally organized thalli with pores occurring mainly on the thicker surface. The thalli are 1.9–3.8 mm wide (mean = 2.68, N = 25) and a few centimeters long. Dichotomous or subdichotomous branching is relatively common. When apices are observed they show the typical rounded morphology of the genus. Pores are circular to slightly oval, 133 to 303 μm in maximum width (mean = 214 μm, N = 48) and have beveled edges. In rare cases the pores can be completely closed by a domed covering. A "cellular reticulum" is present but observed only

in transverse sections of the thalli, making measurements of "cell" dimensions unreliable. Poral surface is 33 to 155 µm thick, while the aporal surface show a thickness of 12–48 µm.

Remarks. We attribute the studied fossils to *Spongiophyton nanum* based on: [1] pore size, which is larger than S. *minutissimum*, but smaller than the up to 800 µm pores of *S. lenticulare*; [2] pore morphology, which is circular to ellipsoid, as opposed to fusiform in *S. lenticulare*, although this could be related to taphonomy; [3] branching is not profuse as reported for *S. minutissimum*; [4] pores almost always with beveled margins; and [5] lack of erect branches (as in *S. minutissimum*). Nevertheless, we note that our specimens have poral and aporal surface thickness with dimensions that overlap those of *S. nanum* and *S. minutissimum*, suggesting that this may not be a reliable character to distinguish both species, if these species are indeed separated taxa and not, for instance, different reproductive stages. Thalli width is another character that shows overlapping ranges between these two species, the exception being *S. lenticulare* with thalli up to 12 mm wide.

Biomineralization

Microparticles and hyphae appear as electron dense areas in ptychography 2D images (fig. S1g,h). EDS point and line analysis of microparticles show compositions similar to low-Mg calcite (fig. S3e). Elevated Ca values are also evident in LA-ICP-MS and ToF-SIMS positive ion spectra (data S1). The correlation matrix (fig. S5) from LA-ICP-MS shows Ca strongly covarying with Sr, as often observed in calcium carbonates. Indeed, the CO_3^{2-} vibrational band is highlighted when the demineralized *Spongiophyton* FTIR spectrum is subtracted from the spectrum of *Spongiophyton* powder further treated with acids (fig. S3c). MicroFTIR maps based on the integrated area from the CO_3^{2-} spectral region show higher intensities at the Ca-rich spots (Fig. 4f; fig. S4g,i,m). The 3.02 Å main peak of calcite appears as a small bump in the SR-XRD diffractograms of *Spongiophyton* (fig. S3a) and pair distribution function (PDF) show a peak at ~3.23 Å that correlate with the combined pair distances of Ca–C, Ca–O and O–O (fig. S3b), as described for crystalline calcite, but not observed in amorphous calcium carbonate (*92*). This confirms a calcite mineralogy, but the lack of long-range order suggests a nanocrystalline nature. SR- and lab-based XRD show the complete absence of calcite in sediments at the fossiliferous level, as well as other levels throughout the outcrop, ruling out incorporation from the surrounding sediment or a diagenetic imprint. The only difference at the *S. nanum* level is the possible presence of siderite (fig. S10), which might have been diagenetic.

Although some of the micrometric calcite crystals seem to show morphological continuity (or absence of defined borders) with the carbonaceous matter, many show the characteristic bipyramidal or bipyramidal-prismatic morphology of biomineralized calcium oxalate (fig. S11). These calcite microparticles are often arranged in layers towards the external surface of *S. nanum* thalli (fig. S12).

Akin to modern cases (*93*, *94*), *Spongiophyton* may have incorporated heavy metals. SR-nanoXRF shows local micrometric spots with clusters of elevated Zn within the fossil (Fig. 4c,e; fig. S2c,h), but some are associated with slight intensities of Ca (fig. S2g,h). These Zn particles are not associated with pyrite since Fe is absent in these spots. Although low Zn concentrations are observed in the LA-ICP-MS (data S1), this is likely due to the localized occurrence of Zn as nano-scale inclusions. From the correlation matrix (fig. S5), it is noticeable that for one of the polished fragments, Zn does not correlate strongly with other more abundant trace metals (although a small covariance is observed for some), but shows a strong correlation with P. This can reflect that the Zn accumulation in *S. nanum* did not occur through particle entrapment, at least

for some of the measured regions. In the second fragment, Zn again only slightly correlates with other trace metals, including Al, which in this case could suggest Zn in trapped particles. Nevertheless, the micrometric Zn particles mapped with SR-nanoXRF do not show other elements that are also present in sedimentary particles or diagenetic pyrite, such as K (many phyllosilicates), Fe, and Ti. The covariation of most trace metals can be attributed to pyrite and occasional phyllosilicate particles trapped by *S. nanum*. Thus, the presence of Zn-rich spots can either indicate zinc oxalate bioprecipitation or bioaccumulation of environmental heavy metal-containing particles (*93*, *94*), both possibilities reinforcing similarities with modern lichens.

In agreement with the LA-ICP-MS, SR-XRD also shows the influence of other minerals, mostly pyrite, but also phyllosilicates. These minerals are inside the thalli of *Spongiophyton* since they appear even in samples prepared with the DSP procedure (see Material and Methods). This means that with the exception of early diagenetic pyrite, they likely reflect very occasional particle incorporation during life, and are likely behind the correlation between some trace metals in the LA-ICP-MS results (fig. S5). Nevertheless, although we can attribute some of the peaks in the SR-XRD to phyllosilicates, they contribute very little to the diffractograms, and SR-XRF elemental map of K (Fig. S2d) indicate just their very occasional occurrence, in opposition to the calcite microparticles.

It is interesting to note that internal granules were observed in Canadian material (*13*). Although there is no chemical or mineralogical information on these inclusions, it is likely that they represent the same type of calcite microparticles after CaOx described here. This reinforces the interpretation of lichen biomineralization rather than a diagenetic origin. To our knowledge, this is the first time that calcite after CaOx has been observed within photosynthetic terrestrial organisms. Although a recent work (*95*) has found globules in Oligocene fossil leaves that the authors interpreted as originally being CaOx, these unusually smoothed structures are now composed of organic compounds, with no traces of calcium minerals. Moreover, some cavities left behind by these globular particles are very similar to impressions left behind by pyrite framboids (Fig. 3e in ref(*95*)). Indeed, the calcium sulphate that occurs near or even surrounding the globules may result from the oxidative alteration of pyrite. Given that the smooth organic globules are believed to have formed after a cavity was left behind, an equally plausible hypothesis is that the initial mineral was not necessarily derived from the plant itself. Instead, it may have been early diagenetic framboidal pyrite, formed due to the anaerobic decomposition of plant tissues. Another evidence in favor of this interpretation is the fact that these globules are not restricted to the fossil leaves, but sometimes also occur scattered in the sediment. Whether these particles are pseudomorphs after pyrite, calcium oxalate, or other minerals requires further investigation.

Organic composition

Elemental analysis, XPS and Rock-Eval parameters reveal a kerogen Type I for *S. nanum*, with atomic H/C ratio of 1.4 and O/C ratios between 0.03 (XPS) to 0.08 (EA), hydrogen index (HI = 1056 mg HC/g TOC) and oxygen index (OI = 0.78 mg HC/g TOC), greenish color under fluorescent light (Fig. 2e,f), and reflectance values of 0.39%. Fitting of the high-resolution C1s XPS spectra also show a low oxygen content, with C-O/C-OH (11.8%), C=O (3.9 %) and O=C-O (2.7%) (Data S1). FTIR parameters of CHal/Ox (1.8) and CHal/C=O (5.1) corroborate a low oxygen content relative to the aliphatic contribution.

The powder diffractograms of *Spongiophyton* show the typical amorphous pattern often observed in previous works with kerogens (*96*), with an intense γ peak attributed to kerogen rich in aliphatic chains. Small broad peaks of aromatics are only discernible in SR-XRD (fig. S3a).

Indeed, our lab-based XRD barely shows the (002) and (100) peaks of aromatic stacking ("graphene band") and in-plane structure of aromatics, respectively (see refs (*96*–*98*)). C-C, C-C-C and C-C-C-C pair distances calculated with PDF are also closer to values from aliphatic chains than aromatic hydrocarbons, even showing similarities to previous experimental PDF of kerogen Type 1 (*99*).

Our XRD-CT images show the spatial distribution of the integrated area of the aromatic and aliphatic peaks. Although for the aliphatic γ peak there is no apparent heterogeneity, this may not be the case for the (002) of aromatic stacks, which show slight variations that could reflect spatial concentration of aromatic compounds. The lack of spatial variation in aliphatic content is also shown by FTIR chemical images (fig. S4). Pyrite grains are clearly discernible in the XRD-CT map based on the (311) reflection of pyrite, and they appear located closer to the lumen between the poral and aporal surfaces.

The ^{13}C CPMAS/TOSS NMR spectrum shown in fig. S6b depicts high intensity in the spectral region associated to aliphatic carbons (10-500 ppm), accounting for a significant aliphaticity (~75%). Most of the signals are related to protonated carbons as they appear heavily attenuated in the dipolar dephased ^{13}C CPMAS/TOSS NMR spectrum, also shown in fig. S13. Interestingly, the peak at ~40 ppm, often attributed to quaternary carbon, may instead reflect N-CHn moieties since this peak disappears in the dipolar dephased spectrum (red in fig. S13). The spectral pattern shown in the 100-160 ppm region suggests the presence of aromatic structures with some degree of condensation or substitution, since there is a predominance of peaks corresponding to signals of non-protonated aromatic carbons, as also shown in the dipolar dephased ^{13}C CPMAS/TOSS NMR spectrum (fig. S13). Nonetheless, the calculated molar fraction of aromatic bridgehead carbon of 0.13 suggests 1-2 aromatic rings per cluster on average, which suggests a higher relative substitution of the aromatic rings rather than condensation.

Both spectra of fig. S6b also depict two signals at 176 and 210 ppm, corresponding to carbonyl carbons, with the signal at 176 ppm accounting for carbonyl esters or amide and the signal at 210 ppm being associated with aldehyde or ketones carbonyl. Indeed, the contribution of N–C=O near 176 ppm may enhance the intensity of the signal in the carbonyl region, which explains the similar intensities of these peaks in the ^{13}C SS-NMR while results from fitting of the XPS C 1s spectra show slightly lower content of COOH/R.

The high aliphaticity observed in the ^{13}C CPMAS/TOSS NMR of *S. nanum* agrees well with results from other techniques employed here. Besides that, the large average methylene chain length and the molar fraction of aromatic bridgehead carbon (data S1) corroborate the low degree of diagenetic thermal alteration as evidenced by elemental and Rock-Eval analysis. This suggests that the alteration of original biopolymers, such as chitin (see below and main text), is more likely to reflect decomposition of *S. nanum* organic matter by microorganisms than a later diagenetic imprint.

Despite the lack of specificity of the N K-edge XANES for the identification of unknown nitrogen functionalities in natural samples, we can draw some general interpretations based on our spectra from *S. nanum* and standards. Firstly, similar to previous works, our spectra are composed of low-energy peaks that reflect 1s to π* electronic transitions (398.6–405 eV), as well as 1s to σ* transitions (>405 eV). The most distinctive peak in *S. nanum* is centered around 400.8 eV, and matches the resonance observed in the melanin standard, suggesting that pyrrole moieties are present. However, similar resonances were reported for pyridones (ref (*100*) and references therein). A pre-edge peak at 398.8 eV confirms the presence of pyridine derivatives in our fossil material, although it can also be partially related to beam damage. In the chitin spectra, we can

observe increasing intensities of resonances near 399 eV and 400 eV following higher X-rays doses. Similar radiation damage was noted before for amino acids (*100*, *101*). There is no discernible peak that can be attributed to amides when compared to the chitin standard, but this peak can be convoluted with the broad pyrrole/pyridones resonance in *S. nanum* spectrum. More interestingly, the main pre-edge peak in the chitosan spectrum shows a shift to higher energies (~402 eV) when compared to chitin, matching the shoulder observed in *S. nanum* at ~402.1 eV. This reinforces the interpretation about the presence of secondary amines in *S. nanum*. Resonances in this range were also previously attributed to amines (*102*). In sum, our N K-edge XANES results broadly correspond to what was observed here with other techniques, although the relative proportion of some nitrogen functionalities are different. This is not new to studies on nitrogen in geologic carbonaceous matter, but it still remains unexplained (*103*).

The C_nN^- peaks observed here in *S. nanum* were also reported from fossil melanosomes (e.g., ref[39]), and in these cases they were interpreted as evidence of melanin preservation, together with other higher m/z C_nN^- fragments. However, other N-rich original sources that undergo polymerization during kerogen formation could also theoretically produce C_nN^- peaks, which is the case for *S. nanum*. Moreover, the presence of the CNO^- peak reinforces a chitin precursor rather than melanin. Although we cannot rule out an original melanin-producing lichen, even more considering that many modern species can produce melanins[40], it seems unlikely that this was the precursor N-rich compound as compared to chitin (or chitosan after it), which is ubiquitous in the walls of fungi hyphae. The low m/z C_nN^- ion fragments observed here and in other studies may not be as specific for identifying compounds as previously considered. Although other higher m/z C_nN^- peaks in *S. nanum* were not observed, this can be related to the monoatomic ion source used.

In the case of melanosomes, the preserved organelle by itself already indicates an original melanin containing compound. However, knowing the original precursor molecule/biopolymer is different from it being preserved in fossil samples. Although it is reasonable to interpret melanin as the original precursor in melanosomes, this is far more complicated in kerogens of unknown or dubious origin. ToF-SIMS cannot confirm the preservation of unaltered or slightly altered melanin or its monomers. Even in cases where melanin is known to have been the precursor given the morphology of the studied structures (i.e., melanosomes), the alternative hypothesis of a melanin-derived, N-rich complex kerogen geomacromolecule that shares little structural similarity with the original melanin cannot be disregarded without more specific methods. Indeed, experimental studies have shown that "eumelanin-specific" ion fragments can still be present in over matured samples, even though structural similarity is lost due to cross-linking and decarboxylation[41]. Thus, as other works have shown[42,43], ToF-SIMS should be complemented with other techniques, especially alkaline hydrogen peroxide oxidation coupled (AHPO) with high-performance liquid chromatography (HPLC). Other methods, such as Raman and FTIR spectroscopy yield indirect evidence of nitrogen functionalities. In our case, the most likely nitrogen-rich precursor was chitin, or chitosan after its decomposition (see main text and below).

Biomarkers of *Spongiophyton* and matrix sediment

i] *n*-alkanes, including waxes

n-Alkanes extracted from the matrix sediment surrounding the fossils show a pronounced odd-over-even predominance (OEP) in the carbon number range C_{12} to C_{18} and again from C_{21} to at least C_{37} (fig. S7b). While the highly abundant waxy *n*-alkanes with OEP in the C_{21+} range may, in principle, derive from leaf waxes of terrestrial plants, the very broad range of OEP carbon numbers does not resemble typical waxes of modern plants. The absence of recognizable fossil

plant debris in the Lower Unit 2 (Alto Garças Sub-Basin) would make plant sources unlikely, although putative fossil plants (i.e., *Octaviona*) are known from coeval deposits in the Apucarana Sub-Basin (*104*). Sedorko et al. (*105*) briefly mentioned the presence of plants in Pragian-Emsian strata from the Lower Unit 2 of the Alto Garças Sub-Basin close to the outcrops studied here, but these were not illustrated. Nonetheless, early vascular plants, such as *Cooksonia,* are known in the older Furnas Formation in southern Brazil (*104*), and possibly even in the correlated units in the Alto Garças Sub-Basin (*85*), both underlying the Pragian-Emsian sediments of the Paraná Basin. Recently, geochemical studies have also found an OEP in the *n*-alkanes in the Alto Garças Sub-Basin (*106*), which led the authors to propose a continental input of organic matter, possibly from land plants, but neither the age of the studied outcrops nor correlation with sub-units of the Alto Garças and Apucarana sub-basins were clarified. Conversely, similarly broad OEP patterns have been observed in marine sediments of Ediacaran age, preceding the colonization of land, and attributed to cyanobacterial and/or microalgal sources (*107*). A cyanobacterial or microalgal source is also a reasonable interpretation for the waxy *n*-alkanes in the matrix sediment here.

The distribution of *n*-alkanes in the solvent extract of the isolated *Spongiophyton* fossil is notably different from the matrix (fig. S7). The carbon number distribution is narrower with a single maximum at C_{15} followed by a rapid decline in concentrations towards higher carbon numbers. Waxy *n*-alkanes with OEP in the carbon number range C_{21} to C_{31} were present in the fossil extract but only detected in trace concentrations.

The *n*-alkane distribution of the fossil pyrolysate is similar to the fossil extract with a unimodal distribution, a maximum at *n*-C_{14} and a rapid decline in concentrations towards higher molecular masses. Notably, while waxy *n*-alkanes are detectable to *n*-C_{31}, they do not possess an OEP.

Waxy *n*-alkanes occur in most or all moderns lichens in highly variable concentrations of 2 to 240 µg/g dry weight (*108*) and with OEP in the C_{23+} range and typically with a particularly strong predominance in the range C_{25} to C_{33}. While it cannot be excluded that the traces of waxy *n*-alkanes in the *Spongiophyton* extract come from the mycobiont itself, it seems more likely that they are derived from the surrounding matrix sediment, as the patterns are very similar (fig. S7). Waxy *n*-alkanes are also strongly resistant to degradation and so it is unlikely that *Spongiophyton* originally possessed a notable *n*-alkane wax coating that was lost during deposition. In conclusion, *Spongiophyton* likely possessed no or only a very minor *n*-alkyl wax protective layer.

ii] Steranes and hopanes

In the sediment matrix, among the three common trifecta steranes cholestane (C_{27}), ergostane (C_{28}) and stigmastane (C_{29}), the C_{29} pseudohomolog is the most abundant (56%) followed by cholestane (25%). Stigmasteroids are also the dominant pseudohomologs among mono- and triaromatic cholesteroids, ergosteroids and stigmasteroids (table S1). Such stigmastane and aromatic stigmasteroid predominances are typical of Palaeozoic bitumens and oils and commonly attributed to chlorophyte algae as dominant eukaryotic primary producers, an interpretation that is also plausible for the sediments studied here. In the extract of the fossil, the absolute concentration of steranes and aromatic steroids was low and the measured pseudohomolog ratios thus not very precise. However, cholestanes (~41%), monoaromatic cholesteroids (~40%) and triaromatic cholesteroids (~38%) are clearly the dominant pseudohomologs. The steranes in the *Spongiophyton* pyrolysate resemble the matrix with stigmastane as the most abundant sterane (~48%) followed by cholestane (29%). In the

monoaromatic steroid fraction, the three pseudohomologs have similar abundances, while triaromatic steroids remained below detection limits.

Differences in sterane and hopane distributions in the fossil extract and pyrolysate confirm the presence of biomarkers covalently bound to *Spongiophyton* organic matter. In the fossil pyrolysate, the relative abundance of eukaryotic steranes to bacterial hopanes (Ster/Hop = 0.03) is ten times lower than in the matrix (0.30) and fossil extract (0.28) (table S1). This is consistent with previous observations that sterols are less readily incorporated into kerogen than hopanepolyols. The isomer distributions of steranes and hopanes are also notably different in the pyrolysate and fossil extract. Diasteranes are below detection limits in the pyrolysate, the stigmastane 20R βαα/ααα ratio is three times higher in the pyrolysate (1.1) than the extract (0.38), and the C_{27} hopane index Ts/(Ts+Tm) points to much lower apparent maturities in the pyrolysate (6.1%) than in the fossil (29%) and matrix (33%) (table S1). The same is observed for the relative abundance of C_{30} moretanes to hopanes with βα/(βα+αβ) = 27% for the pyrolysate, 17% in the fossil extract and 14% for the matrix (table S1). The notably lower isomerization is typical of steranes and hopanes released from kerogen through pyrolysis (*109*). These significant differences between fossil extract and pyrolysate confirm that the biomarkers were generated from the kerogen and not merely desorbed during pyrolysis.

The distribution of C_{27} to C_{35} hopane homologs is also notably different in the matrix and fossil (table S1). In the sediment matrix, C_{29}, C_{30} and C_{31} hopanes have almost equal abundances while C_{27} is lower (C_{27}/C_{30} Hop = 0.62). Conversely, in the *Spongiophyton* extract, C_{27}/C_{30} Hop is three times higher than in the matrix (2.0), and the C_{29}/C_{30} hopane ratio jumps from 1.0 to 1.5. A very similar hopane homolog distribution was also released from the fossil kerogen via pyrolysis, confirming that the hopanes are directly associated with the fossil and are not derived from the surrounding.

iii] Other biomarker features

Apart from the broad OEP *n*-alkane envelope, the matrix sediment did not reveal any conspicuous or unusual hydrocarbon distributions. Carotenoids and aryl isoprenoids of phototrophic sulfur bacteria were not observed, and the homohopane index (HHI) and gammacerane index (GI) were low (table S1), suggesting that the depositional system was neither strongly stratified nor particularly anoxic or sulfidic, consistent with the relatively low organic matter contents and a marginally elevated pristane/phytane ratio Pr/Ph = 3.1. In the fossil extract, Pr/Ph is further elevated (4.7), possibly pointing to longer oxygen exposure time before permanent burial of the *Spongiophyton* specimen.

The 2- and 3-methylhopane indices (2- and 3-MHI) were very low, plant terpenoids generally remained below detection limits, and we did not detect any further biomarkers or unusual ratios that would reveal the activity of specific organisms.

iv] Polar and aromatic compounds in the pyrolysate

The heteroatomic compounds released during pyrolysis of pre-extracted *Spongiophyton* are unusual. Fig. 5f (main text) shows a color-coded total ion current of the pyrolysate, highlighting homologous series of the three main components pyridines (red), alcohols (green) and ketones (blue).

Visible in *m/z* 97 partial mass chromatograms are series of x-hydroxy *n*-alkyl alcohols that possess a single –OH moiety in position x, where x runs from position 2 to the middle of the alkyl chain (Fig. S14a). The relative abundances of the alcohol isomers are subequal, and the carbon

number maximum is at C_{14}. The alcohol series runs to at least C_{29} without a notable even or odd carbon number preference and generally resembles the distribution of the *n*-alkane envelope of the pyrolysate.

The pyrolysate also contains a related series of *n*-alkyl ketones with an oxo-functionality in all positions along the chain. The 2-oxo isomer is the most abundant and 3-oxo the least. Abundances then increase again for ketones with an oxo-group towards the middle of the chain (fig. S14b). Similar to the alcohol series, the ketone series has a maximum at C_{14} and runs to at least C_{23}. In contrast to the alcohol series, the 2-ketones (but not the other isomers) display a slight even over odd predominance between C_{10} and C_{17}, and concentrations drop off markedly after C_{16}.

The most abundant resolved compounds in the pyrolysate belong to multiple series of *n*-alkyl pyridines (figs. S7, S8). *m/z* 121 and 135 partial mass chromatograms show series of pyridines with one *n*-alkyl chain and two and three methyl substituents on the pyridine ring respectively. For both series, the *n*-alkyl chain-length has a concentration maximum at C_6, then drops to C_{11}, rises again to C_{14} and then steeply drops off. Homologs with a side chain longer than 14 carbon atoms only occur in traces.

There are numerous further series with two methyl groups on the pyridine core plus two alkyl chains. For instance, the most prominent series, detected in *m/z* 191, possesses two methyl groups and a pentyl unit on the pyridine ring, as well as an alkyl chain that again has a maximum concentration at C_6 and a drop off after C_{14} (fig. S7a). Equivalent series with two methyl groups and two alkyl chains running from C_2 to at least C_{14} are also all present. Where this is discernible, they all have maxima where the second side chain has six carbon atoms, and a drop-off after C_{14}. The general structure of the pyridine homologous series is thus C_x-(Me_2Pyridine)-C_y, where x and y have a concentration maximum at C_6 and a secondary maximum at C_{14}, while all higher homologs (with C_{14}+ side chains) only occur in traces. The most likely structure based on mass spectra is given in fig. S7a, however the exact attachment points of the methyl groups and side chains on the pyridine core remain to be confirmed with authentic standards.

The *m/z* 134 partial mass chromatogram of the aromatic fraction of the pyrolysate shows a homologous series of trimethyl alkyl benzenes (TMAB (*110*)) that has a maximum at the C_{15} homologue and shows a concentration drop off after C_{23}. As in the pyridine series, this points to a TMAB series where the homologue with a C_6 side chain has maximal abundance, and the concentration drops off after a side-chain length of C_{14}.

v] Diagenesis of *Spongiophyton*

The *n*-alkanes, hopanes and steranes released upon pyrolysis, while clearly chemically bound to *Spongiophyton* organic matter, are likely partially or even predominantly derived from heterotrophic organisms living within or involved in the degradation of *S. nanum* organic matter, plus possible minor contributions of functionalized lipids that diffused into the fossil from the surrounding matrix during early diagenesis.

The three major sterane and monoaromatic steroid homologs (cholesteroids, ergosteroids and stigmasteroid) in the fossil extract and pyrolysate have similar relative abundances and are thus likely the product of mixed sterols sources. Most terrestrial plants have a very strong stigmasteroid predominance while some, such as bryophytes, may contain similar abundances of ergosteroids and stigmasteroids but very little to no cholesteroids. Most fungi and mycobionts of lichens have a strong ergosteroid predominance, and lichen with green algal phycobionts additionally contain substantial amounts of stigmasteroids. Cholesteroids do not seem to play an important role, and are thus not commonly detected in lichens or plants (*111*). Thus, the high

relative abundances of cholesteroids, ~40% in the *Spongiophyton* extract and ~30% in the pyrolysate, may have been contributed by heterotrophic eukaryotes. Conversely, the steroid pseudohomolog distribution in the fossil may also be the result of microbial alteration of the original sterols of *Spongiophyton*. While fossil steroids extracted from quickly buried organisms may faithfully reflect original sterol compositions (*112–114*), extended oxygen exposure before burial may lead to massive loss of indigenous sterols and additionally increase the abundance of cholesteroids relative to stigmasteroids (*42*). Thus, the high relative abundance of cholesteroids in *Spongiophyton* suggests that the original lipids suffered alteration by aerobic degradation and addition of lipids from heterotrophs.

The *n*-alkanes and other *n*-alkyl lipids generated during pyrolysis are likely derived from free fatty acids (FA) and other *n*-alkyl lipids and may not have been part of the macromolecular biomass of *Spongiophyton*. It is well known that FA and other functionalized *n*-alkyl lipids may condense with macromolecular organic matter, partially replacing original biomass. These lipids are then released during pyrolysis of organically preserved fossils as alkanes and/or alkenes. For example, pyrolysis of Silurian and Devonian fossil scorpions predominantly yielded alkanes and alkenes despite the fact that the cuticle of these organisms is composed of chitin without an aliphatic biopolymer component. Pyrolysis of these Paleozoic fossils also did not yield the typical pyrolysis products of modern or subfossil chitin, suggesting that the original chitin in thermally mature samples is largely degraded and partly replaced by lipids (*115*).

A similar origin is likely for the *n*-alkyl lipids in the *Spongiophyton* pyrolysate, including the *n*-alkanes, TMAB, alcohols, ketones, and the alkyl side chain of the pyridines. The unimodal *n*-alkane envelope of the fossil pyrolysate is centered around a concentration maximum (C_{max}) at C_{14}, and the concentrations of *n*-alkanes with higher carbon numbers tail off rapidly. Such an *n*-alkane distribution may originate from FA with 16 and/or 18 carbon atoms, which are the most abundant membrane lipids of most lichens (*111*) and plants, but also of most heterotrophic eukaryotes and bacteria. A similar common precursor is also likely for the TMAB, alcohols, ketones and pyridines. In the pyrolysate, TMAB, *n*-alkanes and alcohols all have concentration maxima at C_{14} or C_{15}. The ketones have a maximum at C_{14} and show a major abundance drop off beyond C_{16}. The *n*-alkyl side chain of pyridines shows a very notable drop off in homolog concentrations beyond C_{14}, and it is likely that tetradecyl was the original substituent before catagenesis and pyrolysis truncated (and partly elongated) the side chain to yield the observed homolog envelope. Furthermore, it is plausible that all *n*-alkyl lipids in the pyrolysate have a diagenetic origin in a simple set of precursor lipids such as common FA. Hypothetically, a fatty acid may have condensed with an N-containing moiety in the macromolecular matrix of *Spongiophyton* and was transformed into thermally stable pyridine during deep burial. It is unknown how *n*-alkyl pyridines form under geological conditions and what type of lipid precursors would yield predominant C_{14} side chains. The precursor may have been a C_{14} lipid (although these are not abundant in nature), but it is also possible that a C_{16} alkyl lipid contributed two carbon atoms to the formation of the pyridine ring, thus creating a C_{14} side chain. Diagenetic experiments will be needed to determine the conditions and components that form these compounds.

vi] Information about the cuticle of *Spongiophyton*

The previous section highlighted that the *n*-alkyl lipids and alkyl side chains in the fossil pyrolysate likely formed by condensation of free lipids with macromolecules of *Spongiophyton*. The pyrolysis of thermally mature, organically preserved fossils generally yields *n*-alkyl compounds, and these compounds do not yield information about polymers and macromolecules

(*115*). By contrast, the unusually abundant and extensive pyridine series in the *Spongiophyton* pyrolysate have, to our knowledge, not been observed before in organically preserved fossils, likely pointing to a nitrogen-rich macromolecular component that reacted with free lipids. The pyridine rings may have formed during pyrolysis from other N-containing precursors, such as chitosan, which is a natural deacetylation product of chitin (see main text). Alternatively, most or all of the detected pyridine moieties may already have formed during diagenesis. The XPS analyses show that pyridine moieties are common in *Spongiophyton* organic matter, contributing 24.5% of all nitrogen in the fossil, together with 25.6% of amines and 24.5% of pyrroles/amides. This confirms that pyridines formed within the sediment during alteration of precursor nitrogenous compounds.

vii] Biomarker syngeneity

In organic geochemical nomenclature, crude oil is 'thermally mature', acknowledging that kerogen in a sedimentary source rock needs to be heated to a minimum temperature and pressure to generate and release hydrocarbons that can migrate into a reservoir. Thus, liquid migrated petroleum, as well as products created from petroleum, always display mature molecular characteristics. By contrast, the biomarkers extracted from the matrix sediment and tissue of *Spongiophyton* are thermally distinctly immature as revealed by sterane and hopane isomer ratios (table S1). This low thermal maturity indicates that these sediments never released hydrocarbons, but it also demonstrates that the biomarkers were not introduced by migrating oil, and they cannot be anthropogenic petroleum products.

Additional evidence for biomarker syngeneity comes from a comparison of fossil extract and pyrolysate. Kerogen is a solid organic phase that cannot migrate and is thus always an indigenous phase of sedimentary rock. Hydrocarbons released from kerogen by cleavage of covalent bonds are thus also considered indigenous. While the pyrolysis of kerogen may release strongly adsorbed contaminants, genuine pyrolysis products can be recognized using diagnostic patterns. Such patterns are clearly present in the *Spongiophyton* pyrolysate: loss of *n*-alkane carbon number preference caused by C-C bond cleavage (fig. S7), a strongly depressed sterane / hopane ratio, and sterane and hopane isomer ratios that point to an apparent lower maturity in comparison to free hydrocarbons in the fossil (bound biomarkers are protected from isomerization). These characteristics show that the hydrocarbons were cleaved from the solid organic matter of *Spongiophyton* and are not migrated oil or contaminants.

Previous chemical investigations of *Spongiophyton*

Chaloner et al. (*43*) and Gensel et al. (*13*) reported the first elemental analysis from this fossil. The nitrogen content of *S. nanum* in Chaloner et al. (*43*) agrees well with our data, although *S. minutissimum* showed lower nitrogen content (*13*). Whether this difference is related to original composition or later loss of heteroatoms during diagenesis remains to be evaluated. Yet, it is interesting to note that other occurrences of this genus also show a nitrogenous-rich composition that is unlike those of reported early land plants. Subsequent works investigated the bulk molecular composition of this fossil and showed closer compositional similarities to recent and fossil algal matter (i.e. *Botryococcus*) than with known fossil plants (*116*, *117*). Interestingly, *Nematothallus* also clustered together with *Spongiophyton* closer to algae and fossil algae. The low concentration of aromatic aldehydes in these fossils was further suggested to differentiate them from plants (*116*). However, these early studies did not fully consider the impact of heterotrophic reworking on the

molecular composition of fossils. Heterotrophs may extensively alter the original lipid pool, replacing it with their own lipids, thus complicating the chemotaxonomy of fossils.

More recently, Gaia et al. (*15*) provided further chemical information on *Spongiophyton* using EDS and FTIR. However, EDS is widely recognized as an inadequate method for kerogen analysis given its low sensitivity for light elements. Furthermore, surface measurements on carbonaceous fossils that have not undergone acid treatment will likely have a contribution from attached impurities of the surrounding host rock. This contamination is attested by the presence of Si and Al in point analysis results of the fossils. Gaia et al. (*15*) attributed the predominance of C and O in *Spongiophyton* to "the most volatile elements of the original organic matter in the plant cuticle [being] dissipated into the atmosphere, increasing the C concentration and resulting in fossilization by carbonification." However, it is unclear what the authors meant by this statement. Typically, the transformation of organic matter into kerogen involves diagenesis and metamorphism, leading to aromatization and the loss of volatiles and heteroatoms.

Further challenging interpretations by the authors include the fact that oxygen in both fossil and host rock was interpreted as being an "atmospheric component," which is difficult to reconcile with the high oxygen content observed, even when using an environmental SEM. Nonetheless, contrary to their own statement, the authors then proceed to interpret the oxygen content as indeed pertaining to the fossils and minerals further on in the text.

The interpretation about calcium in the EDS results also raises questions. The authors also found a small percentage of calcium (1.38wt% and 2.87wt%) in point analysis of the fossils. Despite the low values, the authors stated that the Ca peaks in the spectra were more intense than the O peaks (Figs. 4B and 5B of Gaia et al. (*15*)). This reflects a misinterpretation of Ca L-shell emission lines, which overlap with the C K-shell emission lines. Given the weak Ca signal and potential contamination, it is unclear whether the Ca originates from the same type of calcite inclusions reported here or from surface contamination.

The FTIR results in Gaia et al. (*15*) are also problematic. These are dominated by well-known peaks of mineral matter (mostly silicates) and were erroneously interpreted as organic functional groups. For instance, the peaks around 1000 cm^{-1} and below 500 cm^{-1} (near 470 cm^{-1}) reflect the Si-O-Si stretching and bending vibrations of phyllosilicates, respectively (*118*, *119*). The presence of phyllosilicates is further corroborated by the presence of a peak near 900 cm^{-1} that can be assigned to the AlOHAl bending. These infrared bands not only occur near the same wavenumbers, but they also share the same overall spectra profile as in the spectra of silicates. Consequently, no reliable conclusions regarding the organic chemistry of *Spongiophyton* can be drawn from these data. Notably, the well-known CO_2 peak, a common contamination from gaseous carbon dioxide present along the beam path during laboratory FTIR analysis, remained unidentified by the authors.

Matsumura et al. (*120*) have also studied *Spongiophyton* (from the Apucarana Sub-Basin, Paraná Basin) using diffuse reflectance FTIR, and reported semi-quantitative values calculated from the resultant spectra. In particular, their CHal/Ox values are much lower than observed here. This can be explained in part by the method employed (diffuse reflectance vs transmission mode) and possibly spectra processing procedures, such as baseline correction, the latter likely influencing how much of the area is integrated below the peaks. More importantly, here we show that there is a mineral contribution from inside these fossils. This prevents a more accurate investigation of their organic composition unless the remains are further processed to better remove mineral particles inside the lumen (i.e., sediments) and the organic tissue (i.e., calcite particles and pyrite). Even if such care is taken, mineral particles can still remain if they are

abundant, small, and deep within the organic remains. Thus, it is unclear if FTIR parameters can be confidently compared between works, since there may be variations in sample preparation, remaining mineral contamination, and varying acquisition modes and spectral processing methods. Nonetheless, using the indirect "A factor" and "C factor" parameters of Ganz and Kalkreuth (*121*), Matsumura et al. (*120*) suggested that the analyzed *Spongiophyton* remains should be grouped among the range of values of kerogen Type II, and even kerogen Type III, but no complementary elemental or Rock-Eval analysis was included to support these conclusions. Their interpretation about the nature of *Spongiophyton* kerogen type is not only different from the results of the combined techniques here, but also disagrees with the H/C and O/C ratios closer to kerogen type I calculated from the elemental composition of *Spongiophyton* reported by Chaloner et al. (*43*).

Occurrence and paleogeographical distribution

Spongiophyton is often considered as having a cosmopolitan distribution during Early to Middle Devonian, ranging in time from the Pragian to the Givetian. We accurately evaluated the paleogeographic distribution of this fossil by compiling all valid occurrences reported in the literature. Occurrences that were very close to each other were plotted as one in the paleogeography reconstruction. The compiled information was used in GPlates 2.3.0 using the paleogeographic dataset from Merdith et al. (*84*). Although *Spongiophyton* ranged in time approximately 30 million years (Pragian to Eifelian-Givetian), for simplicity we show its distribution in the estimated paleogeography at 400 Ma, which is closer to the age of most occurrences.

Considerations about some of the occurrences also need to be made, and we stress the need for a review in the future. Although Gensel et al. (*13*) had raised questions about the assignment of Zdebska's (*122*) material (Devonian of Poland) to this genus, recent illustrations of *Spongiophyton* sp. 1 more clearly show the distinct pore type, dichotomous branching and the rounded apices (*123*). Thus, we retain this occurrence here, but we agree with Gensel et al. (*13*) and Edwards (*124*) that *Spongiophyton* sp. 2 more likely represents *Nematothallus*. We also consider the Chinese occurrence of *Spongiophyton* contentious. These fossils were referred as thick cuticles with pores and tentatively assigned to this genus (*125*). Indeed, the illustrated specimens and schematic drawings show pores with similar sizes to those reported for *S. minutissimum*, and apparently with beveled edges (Plate III-Figs 10,11 in ref(*125*)), but there is no information on branching morphology, apices outline, presence of a "cellular reticulum", and dorsiventral organization. Thus, we consider these fossils as putative occurrences of *Spongiophyton*. Finally, the material reported from Bolivia by Boureau and Pons (*126*) is considered a valid occurrence, but its age is contentious. In their work, the exact location and the geological unit of this fossil is not presented. Boureau and Pons' (*126*) material was collected between Tarjita and Azurduy, in the Interandean of Bolivia. An Emsian invertebrate assemblage from the Icla Fm is known from the Azurduy-San Roque (*127*) region and it is possible that these successions correlate with the location of the *Spongiophyton* specimens. Thus, we preliminarily consider an Emsian age for this occurrence, although future work should further explore its age. Nevertheless, *Spongiophyton* was also found in younger rocks from the Los Monos Fm (Givetian-Frasnian) in southern Bolivia (*128*).

Our paleogeographical plots confirm the worldwide distribution of this genus, from latitudes of almost 80° S to close to the equator (c. 22-7° S) (Fig. 6). The cosmopolitan nature suggests a broad temperature tolerance for *Spongiophyton*, and also physiological capabilities to deal with different humidity regimes. Moreover, its latitudinal distribution coupled with their high abundance in some of these strata demonstrate that lichens were not only present at this time but

heavily contributed to the biomass of terrestrial ecosystems. Finally, no special pattern of dispersion is evident. Already by the Emsian there are occurrences of *Spongiophyton* in Gondwana and Laurussia. Nevertheless, the Pragian-Emsian age of the succession studied here, the Pragian-Emsian age of Moroccan *Spongiophyton* (*129*), and the possible Emsian age of some Bolivian occurrences shows that *Spongiophyton* most likely originated in Gondwana at high latitudes, instead of Laurussia, as previously considered (*130*).

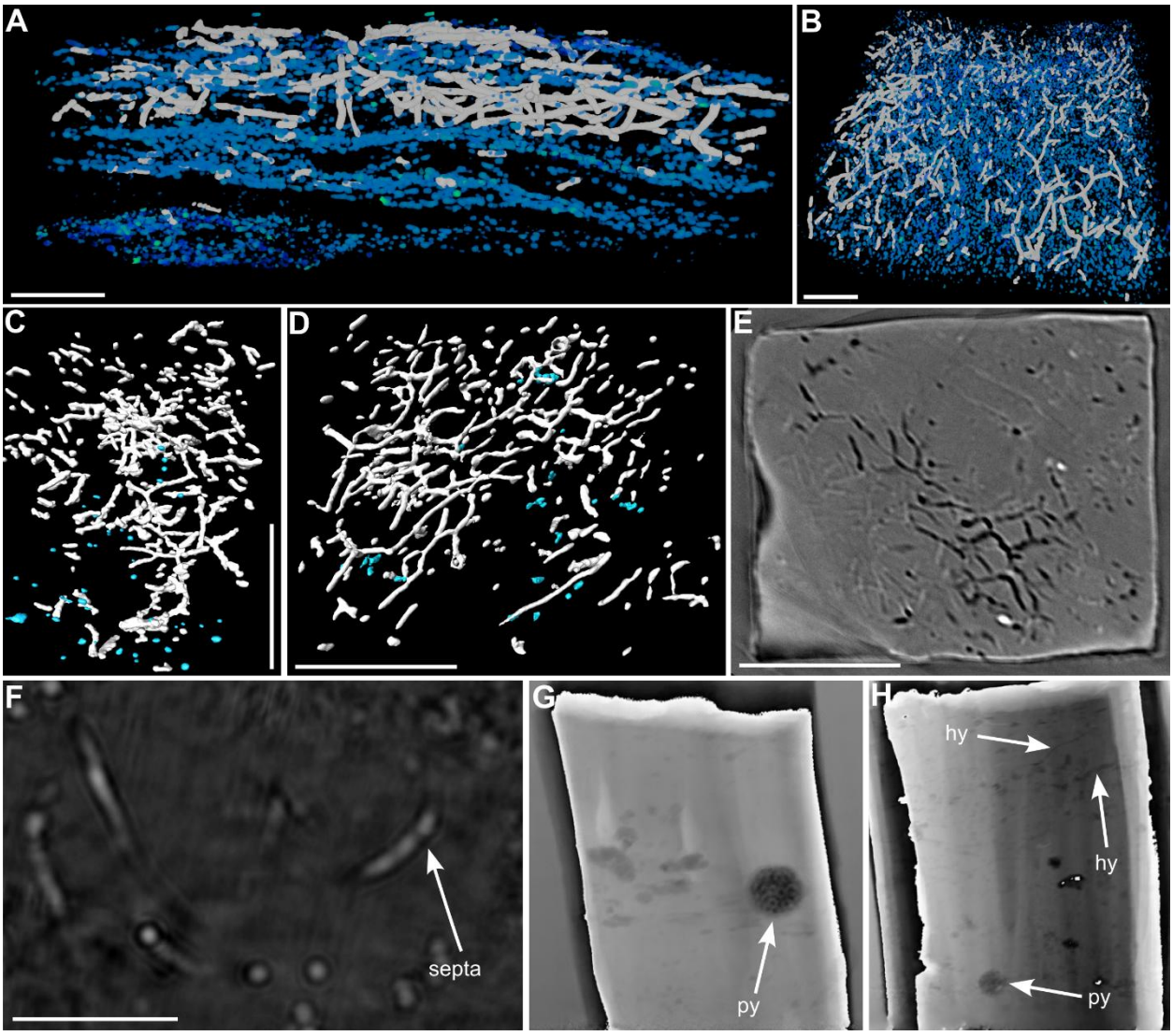


Fig. S1. SR-nanoCT and 2D ptychography. **a,b**, Distribution and orientation of hyphae parallel to the surface, alongside microparticles of calcite (blue) concentrated at the outermost portions of the aporal and poral surface. **c,d**, Label image of other samples showing hyphae and calcite particles. **e**, Slice of a small sample treated with HF and HCl showing the dissolved and non-dissolved calcite-preserved hyphae. **f**, detail of hyphae showing signs of septa (arrow). **g,h**, 2D ptychography highlighting the electron dense hyphae and occasional framboidal pyrite within ~25 µm columns. Scales: 50 µm (**a, b**); 100 µm (**c-e**); 30 µm (**f**).

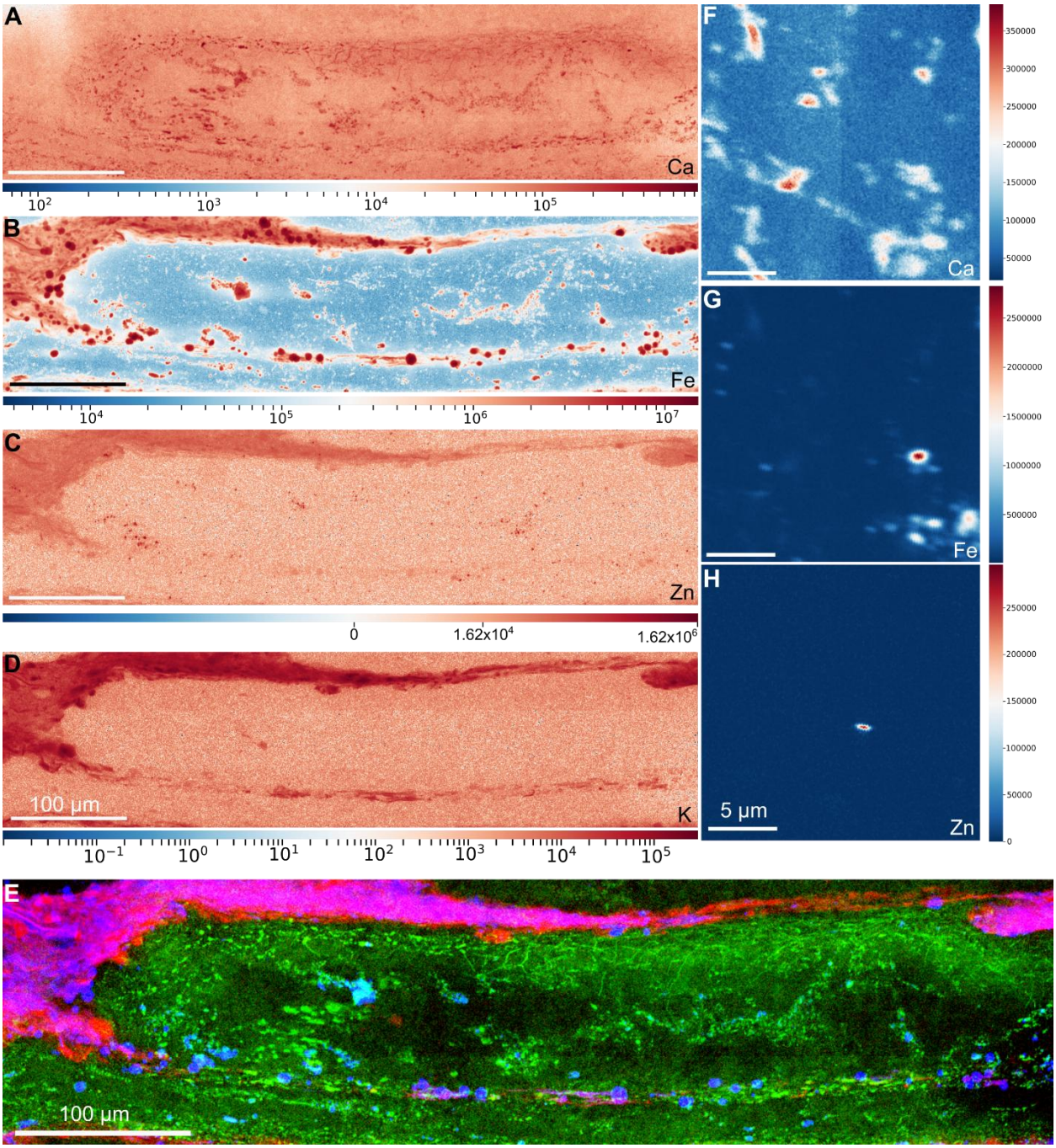


Fig. S2. Synchrotron micro- nanoXRF maps. **a-d**, Log-scale nanoXRF maps of Ca (**a**), Fe (**b**), Zn (**c**), and K (**d**). **e**, Composite map showing Ca (green), Fe (blue), and K (red). **f-h**, high-resolution (100 nm pixel size) nanoXRF maps of Ca (f), Fe (g), and Zn (h).

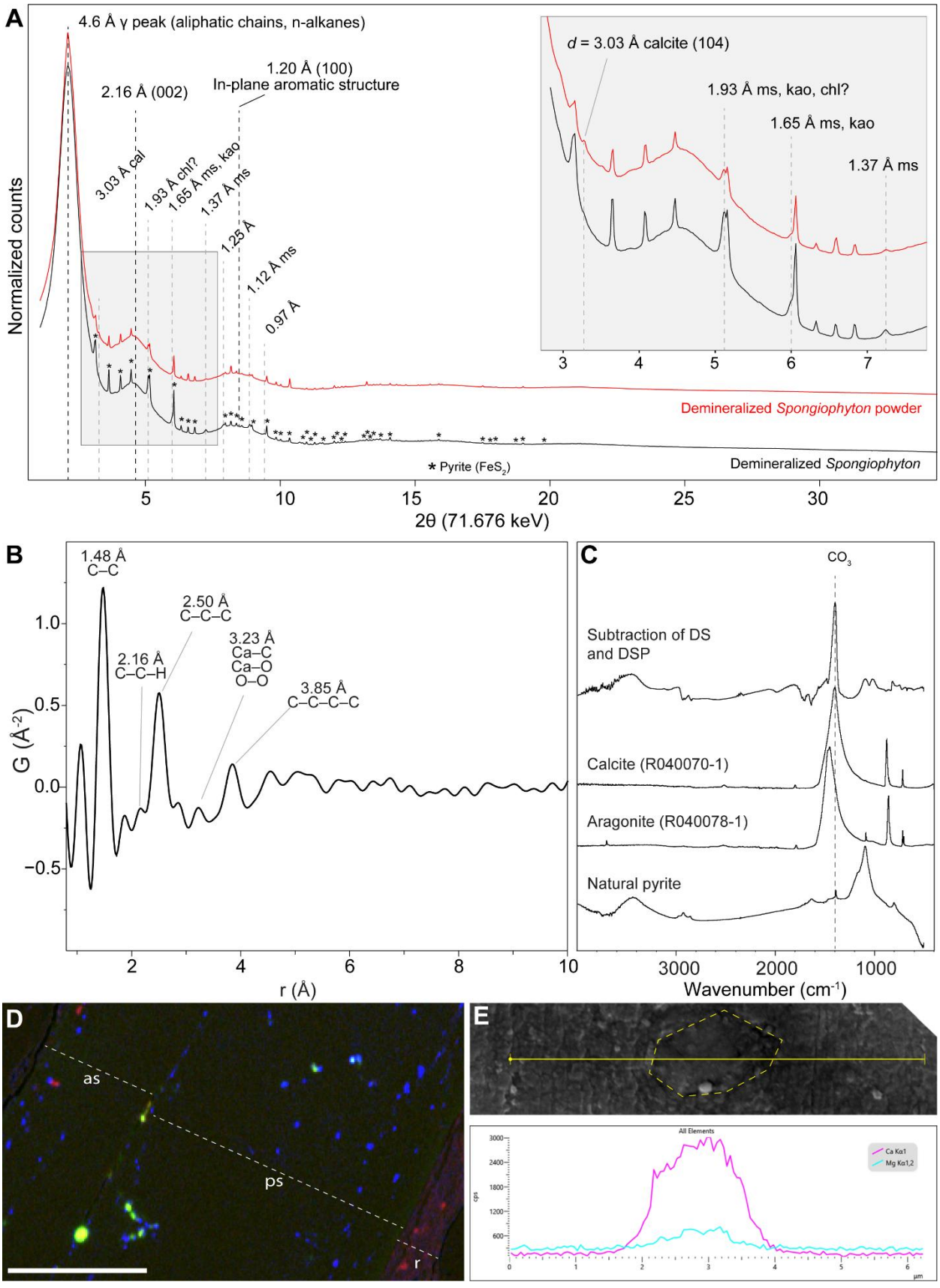

A
4.6 Å γ peak (aliphatic chains, n-alkanes)
2.16 Å (002)
1.20 Å (100)
In-plane aromatic structure
3.03 Å cal
1.93 Å chl?
1.65 Å ms, kao
1.37 Å ms
1.25 Å
1.12 Å ms
0.97 Å
d = 3.03 Å calcite (104)
1.93 Å ms, kao, chl?
1.65 Å ms, kao
1.37 Å ms
Normalized counts
Demineralized Spongiophyton powder
* Pyrite (FeS2)
Demineralized Spongiophyton
2θ (71.676 keV)
B
1.48 Å
C–C
2.50 Å
C–C–C
3.23 Å
Ca–C
Ca–O
O–O
2.16 Å
C–C–H
3.85 Å
C–C–C–C
G (Å-2)
r (Å)
C
CO3
Subtraction of DS
and DSP
Calcite (R040070-1)
Aragonite (R040078-1)
Natural pyrite
Wavenumber (cm-1)
D
as
ps
r
E
All Elements
Ca Kα1
Mg Kα1,2
cps
μm

Fig. S3. Mineralogy, short range structure, and molecular and elemental composition of *S. nanum*. **a**, SR-XRD diffractograms for demineralized *Spongiophyton* powder and demineralized *Spongiophyton* showing the intense broad aliphatic and small broad aromatic peaks. Most Bragg peaks result from pyrite (*), although a few can be attributed to muscovite (ms), but also possibly kaolinite (kao), and chlorite (chl). **b**, Pair distribution function graph showing the main pairs of distinguished peaks occurring up to 4 nm, then dampening around zero, as expected for an amorphous or nanocrystalline material. **c**, Subtraction of the spectra from the two differently prepared samples (demineralized *Spongiophyton* [DS] and demineralized Spongiophyton powder [DSP]) highlighting the disappearance of the carbonate vibration in the sample with further demineralization. **d**, EDS elemental map of iron (red), sulfur (green) and calcium (blue). **e**, EDS line measurement through a micrometric Ca-rich particle with euhedral shape, with the electron image (above) and intensity of Ca and Mg along the line.

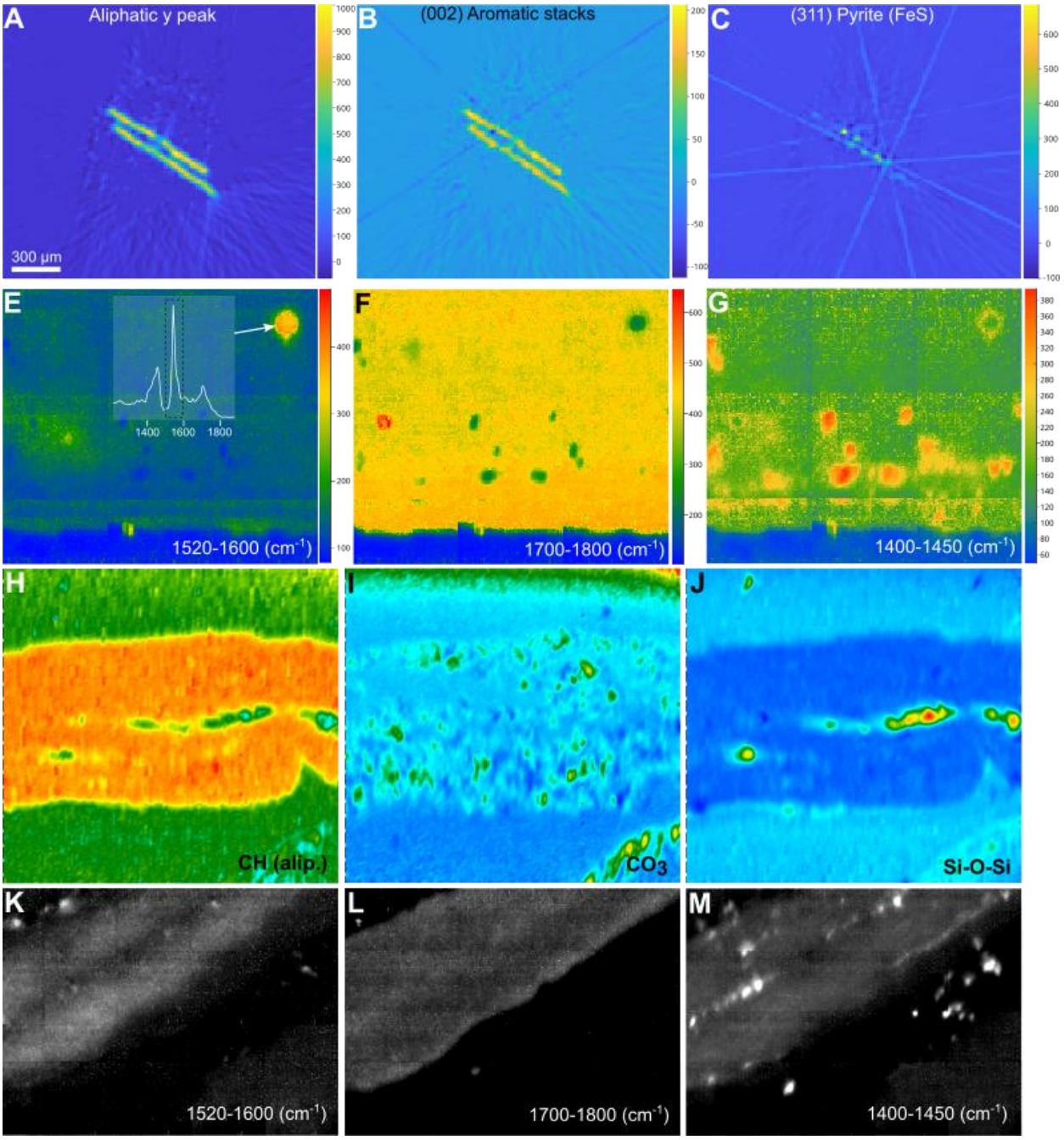


Fig. S4. Chemical and structural heterogeneity of *S. nanum* demonstrated by X-ray diffraction tomography (XRD-CT) and FTIR chemical maps. **a-c**, Intensity maps based on selected 2θ regions that highlight spatial variations in the aliphatic (a) and aromatic components (b), as well as the presence of pyrite grains towards the lumen. **e-m**, microFTIR of polished longitudinal sections showing maps of C-N/N-H (**e,k**), C=O (**f,l**), CO3 (**g,i,m**) and Si-O-Si (**j**).

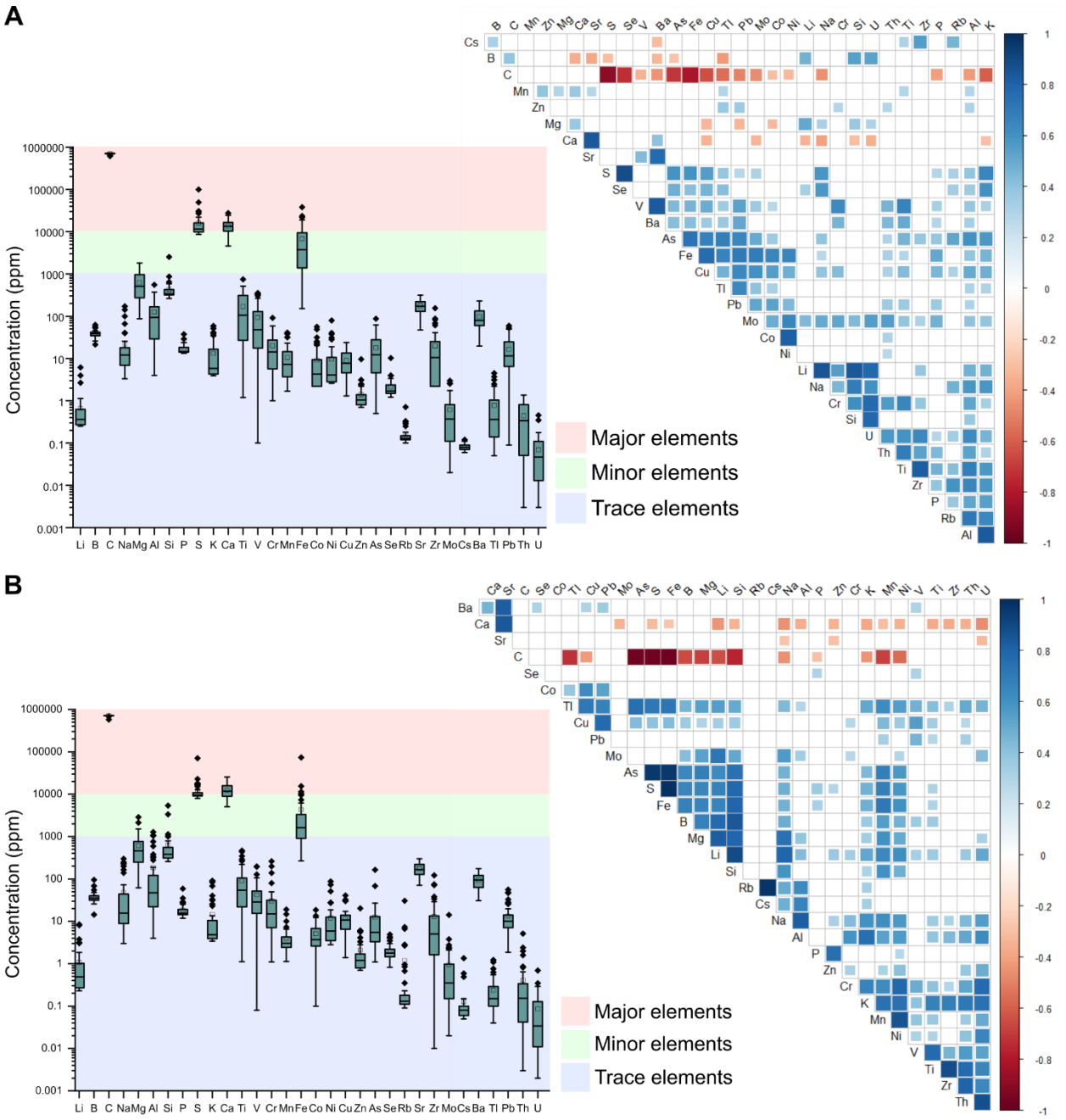


Fig. S5. LA-ICP-MS analysis of *S. nanum*. To the left: concentrations of measured elements in two (**a** and **b**) polished longitudinally sectioned thalli. To the right: correlation matrix with hierarchical clustering based on the LA-ICP-MS results.

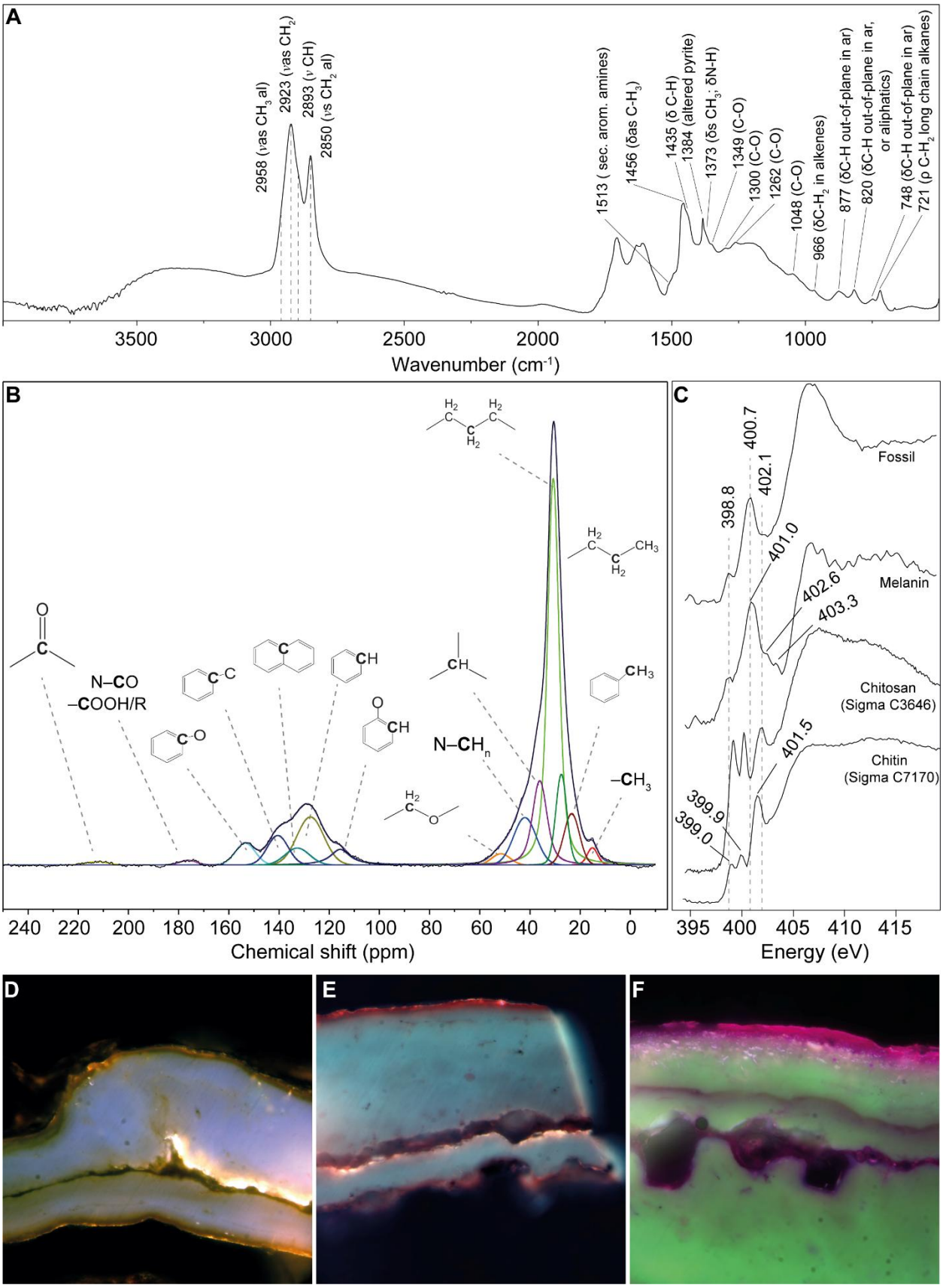

A
2958 (νas CH3 al)
2923 (νas CH2)
2893 (ν CH)
2850 (νs CH2 al)
1513 (sec. arom. amines)
1456 (δas C-H3)
1435 (δ C-H)
1384 (altered pyrite)
1373 (δs CH3; δN-H)
1349 (C-O)
1300 (C-O)
1262 (C-O)
1048 (C-O)
966 (δC-H2 in alkenes)
877 (δC-H out-of-plane in ar)
820 (δC-H out-of-plane in ar, or aliphatics)
748 (δC-H out-of-plane in ar)
721 (ρ C-H2 long chain alkanes)
3500
3000
2500
2000
1500
1000
Wavenumber (cm-1)
B
N–CO
–COOH/R
N–CHn
–CH3
240 220 200 180 160 140 120 100 80 60 40 20 0
Chemical shift (ppm)
C
Fossil
Melanin
Chitosan
(Sigma C3646)
Chitin
(Sigma C7170)
398.8
400.7
402.1
401.0
402.6
403.3
401.5
399.9
399.0
395 400 405 410 415
Energy (eV)
D
E
F

Fig. S6. Spectroscopic analyses of *S. nanum*. a, Lab-based FTIR spectrum from the *Spongiophyton* demineralized powder (DSP) with band assignments. **b**, Fitting of ^{13}C CP/TOSS NMR. **c**, Nitrogen K-edge XANES. **d-f**, Multispectral luminescence microscopy of *S. nanum* thin sections highlighting chemical heterogeneity within the thalli, especially towards the upper cortex. Wavelengths and filters used are: (**d**) 385 nm (514, 650, 835 filters); (**e**) 385 nm (458, 514, 835 filters); and (**f**) 460 nm (514, 650, 835 filters).

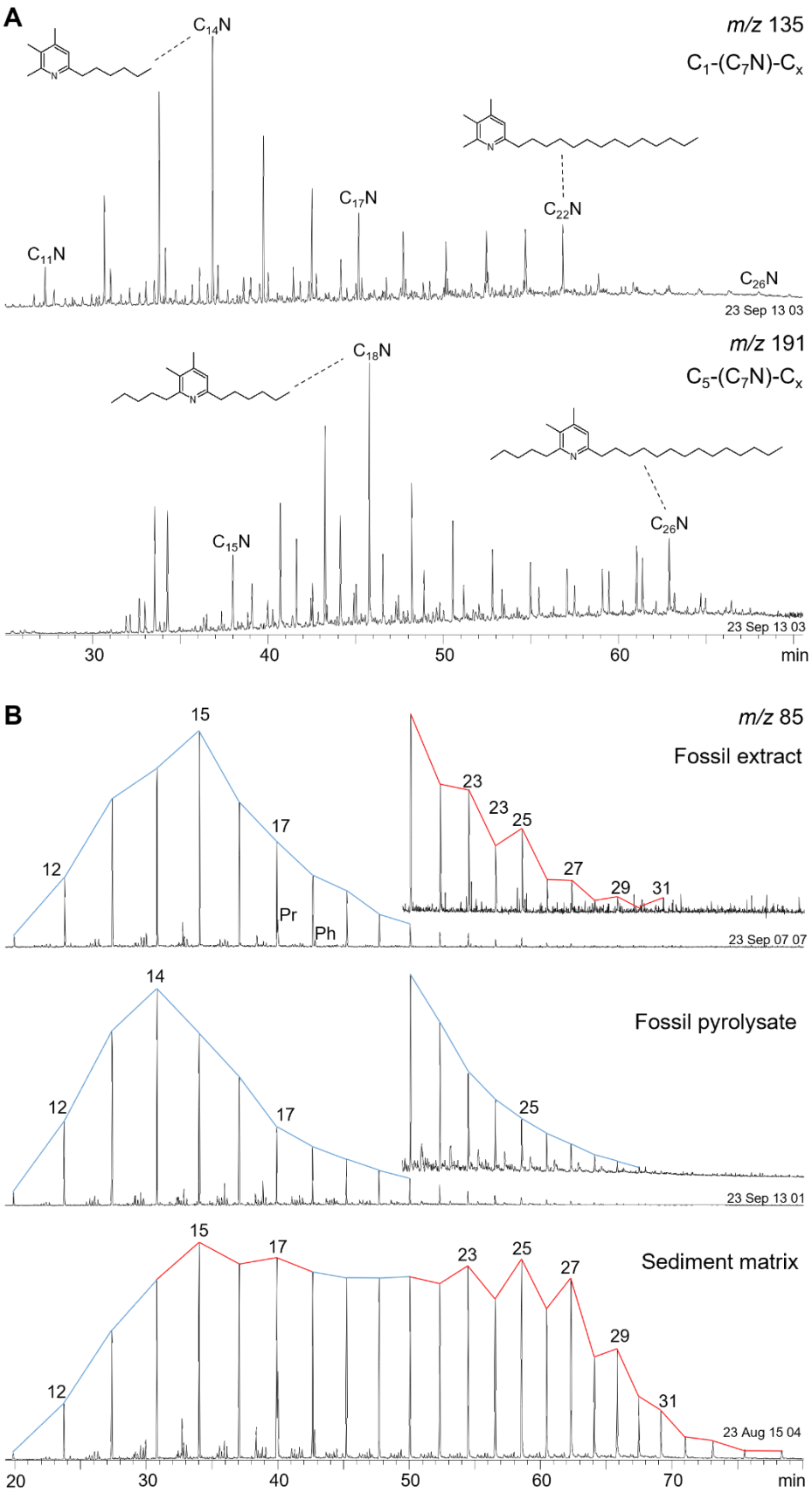

A
m/z 135
C1-(C7N)-Cx
C14N
C17N
C22N
C11N
C26N
23 Sep 13 03
m/z 191
C5-(C7N)-Cx
C18N
C15N
C26N
23 Sep 13 03
30
40
50
60
min
B
m/z 85
Fossil extract
15
17
12
Pr
Ph
23
23
25
27
29
31
23 Sep 07 07
Fossil pyrolysate
14
12
17
25
23 Sep 13 01
Sediment matrix
15
17
23
25
27
29
12
31
23 Aug 15 04
20
30
40
50
60
70
min

Fig. S7. Molecular composition of the fossil extract and pyrolysate of *S. nanum* and its sedimentary rock matrix. a, Partial m/z 135 and 191 mass chromatograms of the polar fraction of *S. nanum* pyrolysate highlighting two n-alkyl pyridine series displaying a maxima at an n-alkyl side-chain length of C6 and a sharp concentration decline beyond a side-chain length of C14. Also present, but not shown, are all additional pyridine series Cx (C7N) Cy with x and y = 0 to 14. Shown are the most likely chemical structures based on mass spectra but note that the precise position of the side chains and methyl groups has not been confirmed using authentic standards. b, Partial m/z 85 mass chromatograms showing n-alkane homolog series. n-Alkane regions without carbon number preference are highlighted in blue and with odd-over-even predominance in red. Alkanes are identified by carbon number. Pr = pristane, Ph = phytane.

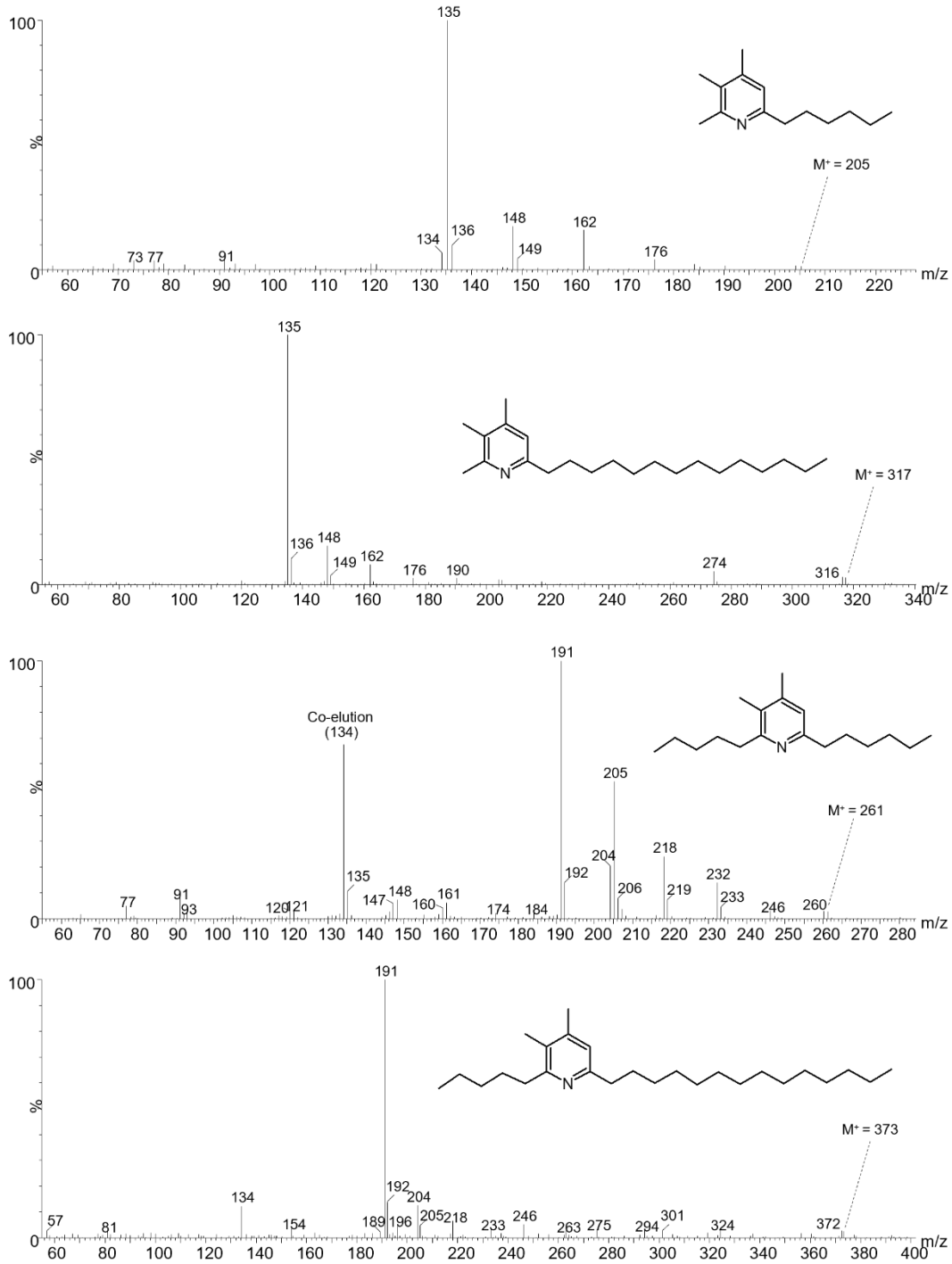


Fig. S8. EI+ mass spectra of alkyl pyridines labelled in Figure S7.

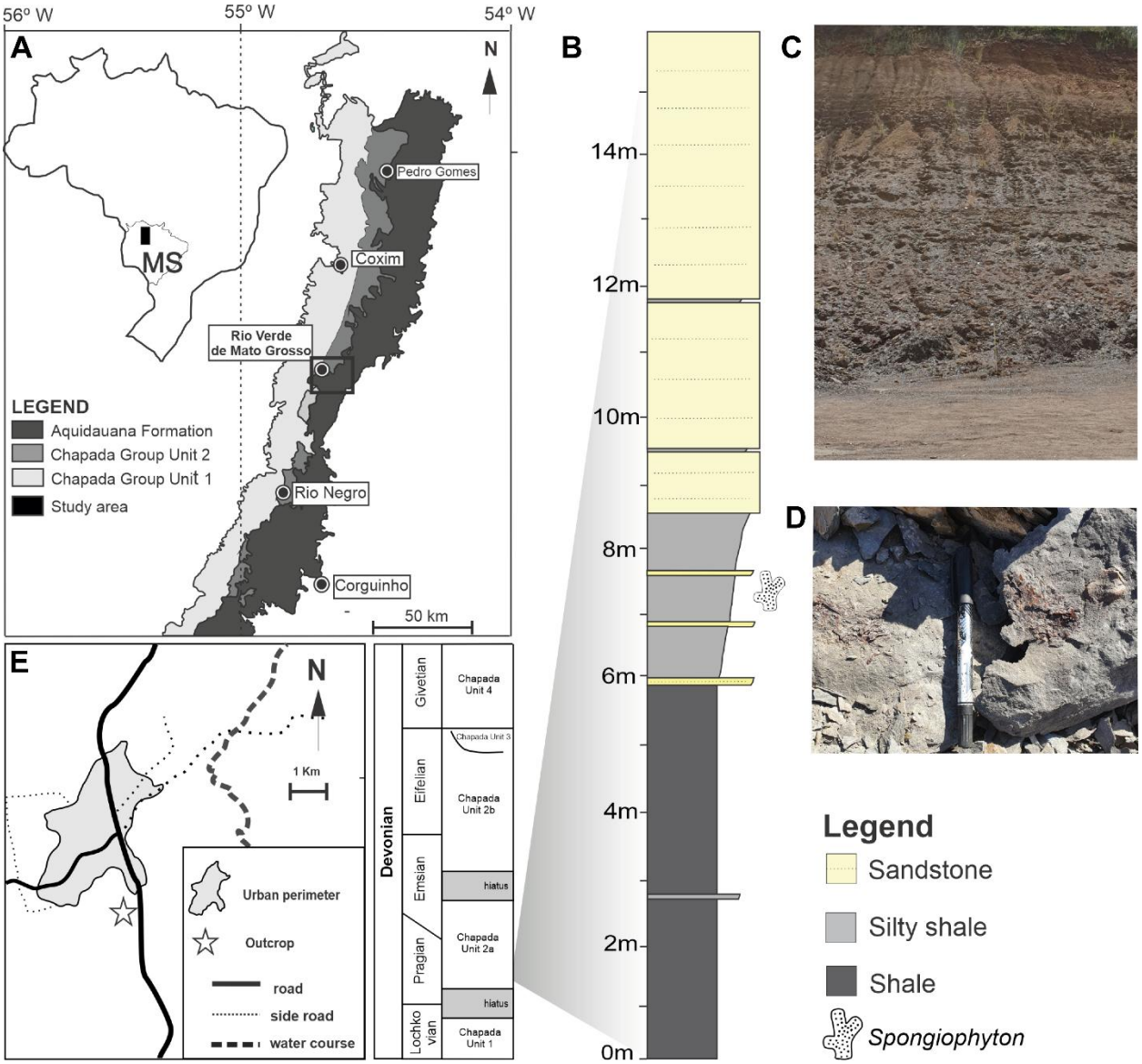


Fig. S9. Geological context of the studied material. a, Location, and geological map of the investigated Devonian successions in Mato Grosso do Sul State, Brazil. **b**, Location of the outcrop near Rio Verde de Mato Grosso city. **c**, Stratigraphic log of the outcrop. **d**, Field photograph showing the fine-grained sediments at the base grading to coarser sediments upsection. **e**, Field photograph of the studied sample before collecting.

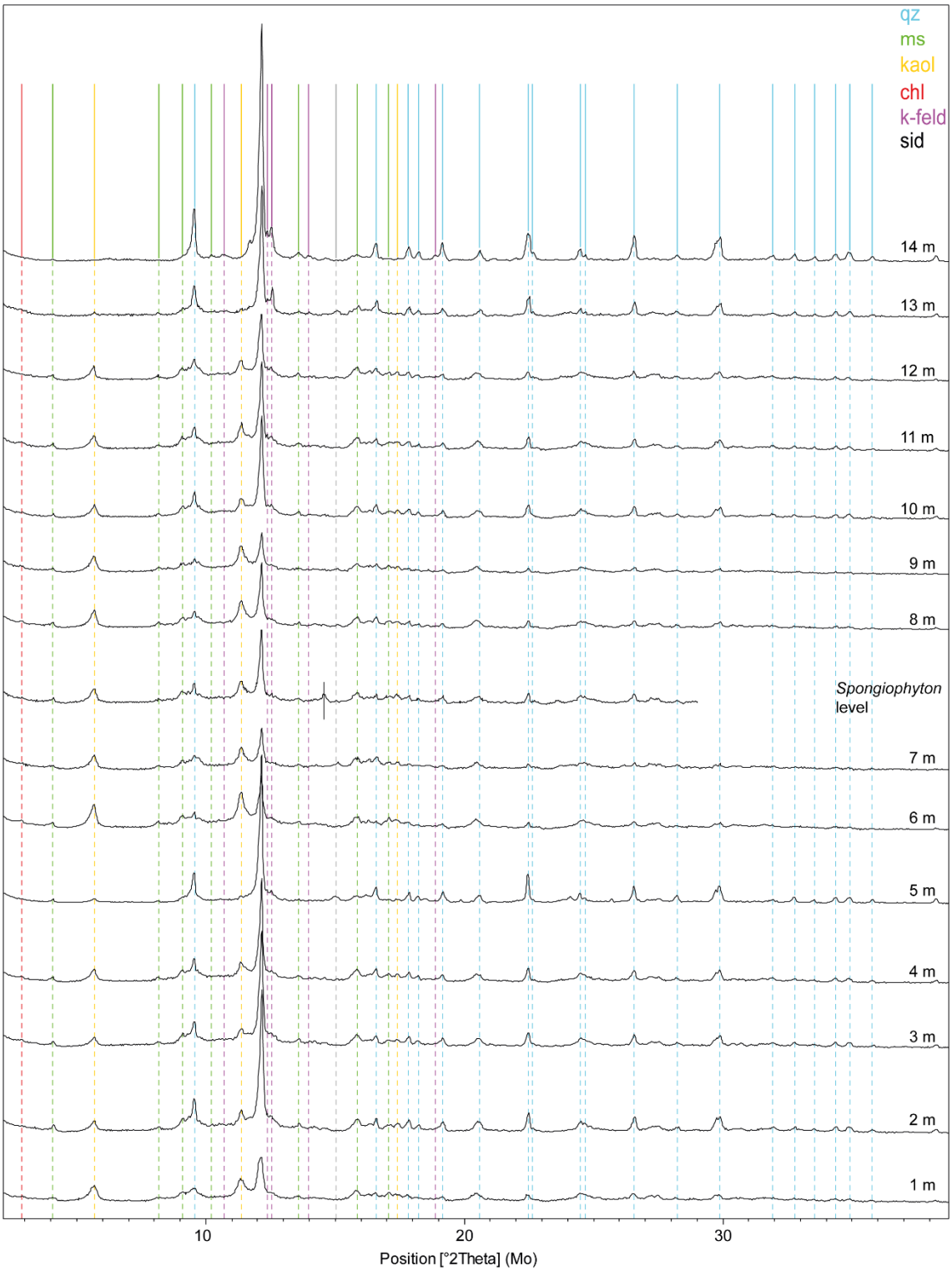


Fig. S10. Lab-XRD of host rock in distinct levels throughout the outcrop. No calcite peaks are observed in all the horizons. Major minerals include quartz (qz), muscovite/illite (ms), and kaolinite (kaol). Minor phases include chlorite (chl), k-feldspars (k-feld), and siderite (sid; at the *S. nanum* level only).

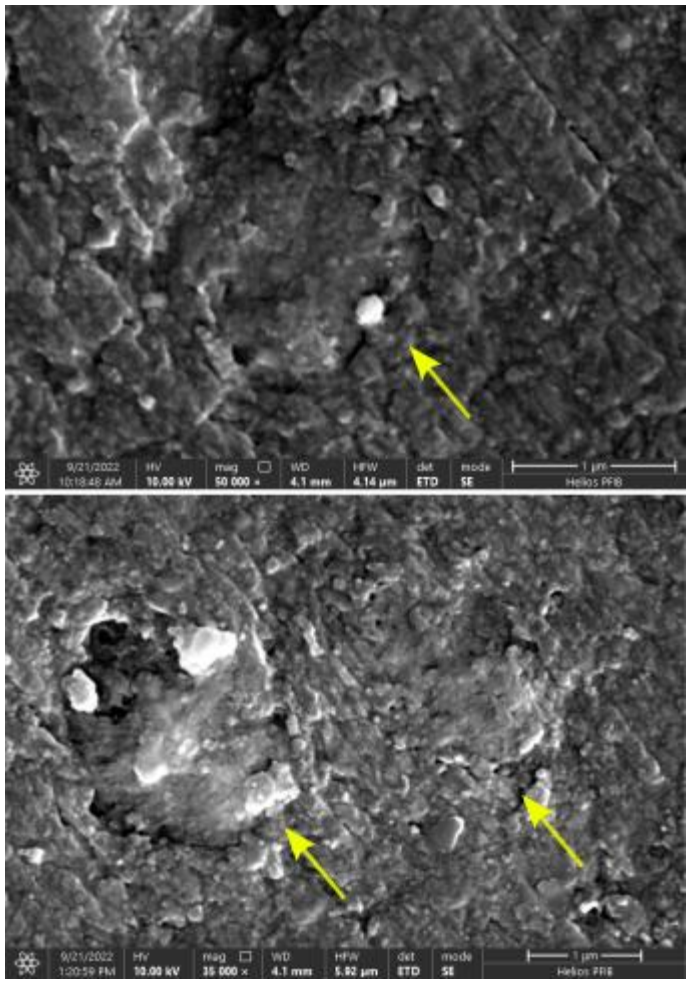


Fig. S11. Secondary electron image of calcite microparticles within *S. nanum*.

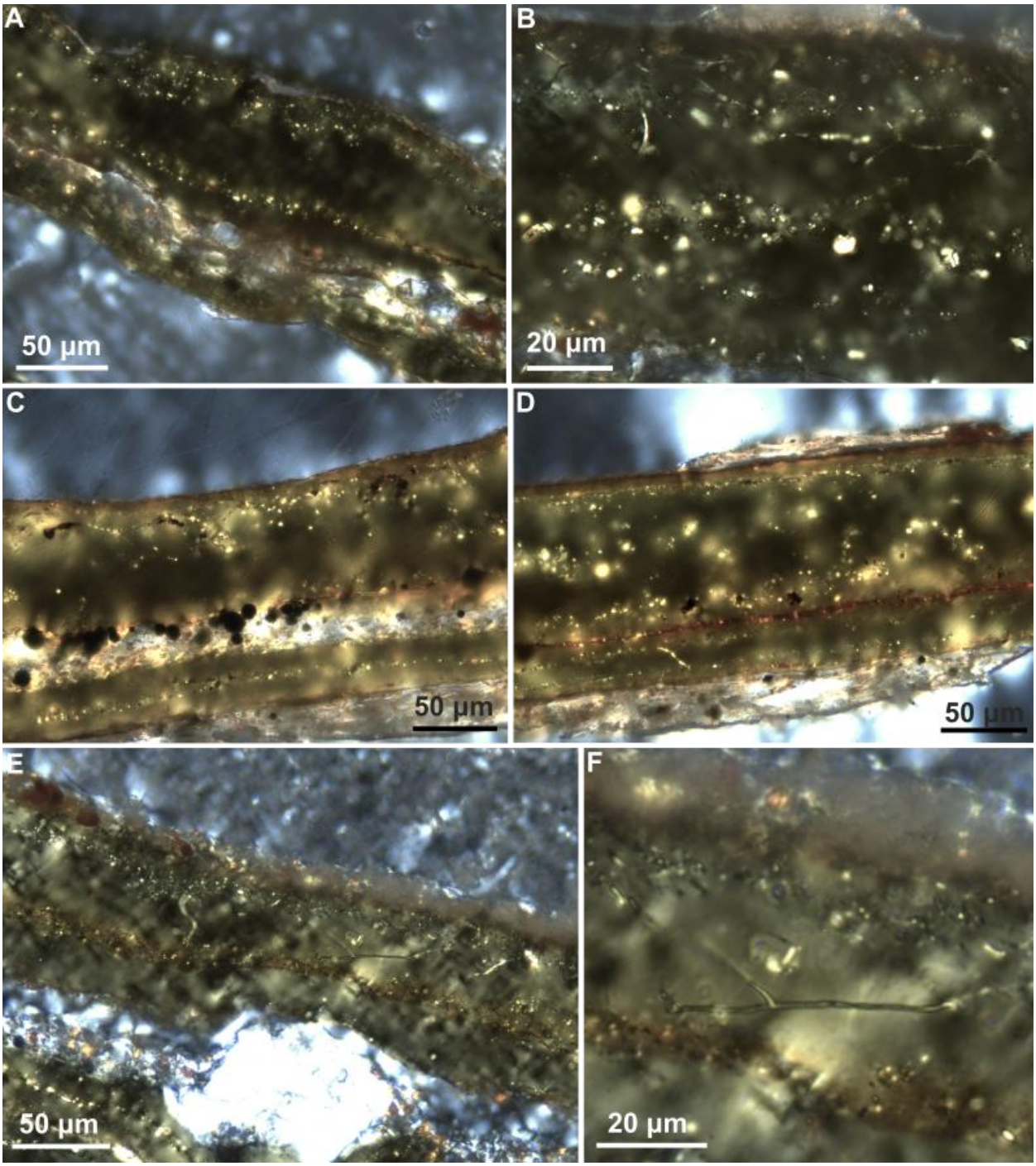


Fig. S12. Calcite microparticles and hyphae. a-f, Concentration of calcite microparticles towards the outer border of poral and aporal surfaces. **c,d**, Framboidal pyrite concentrated towards the lumen. **e**, bifurcating hyphae. **f**, detail of (**e**).

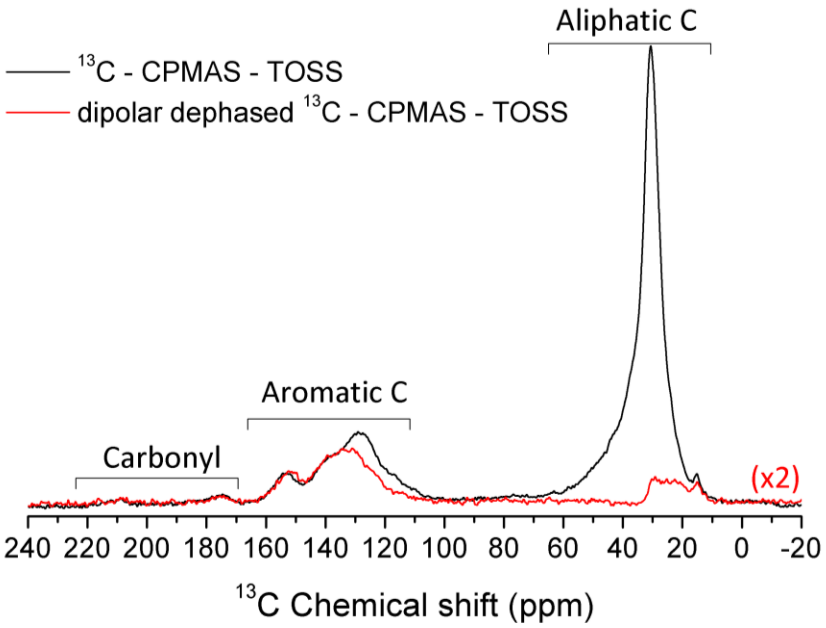


Fig. S13. ^{13}C CPMAS/TOSS NMR spectra of *Spongiophyton* powder (black) and dipolar dephased ^{13}C CPMAS/TOSS NMR spectra (red) of *Spongiophyton* powder.

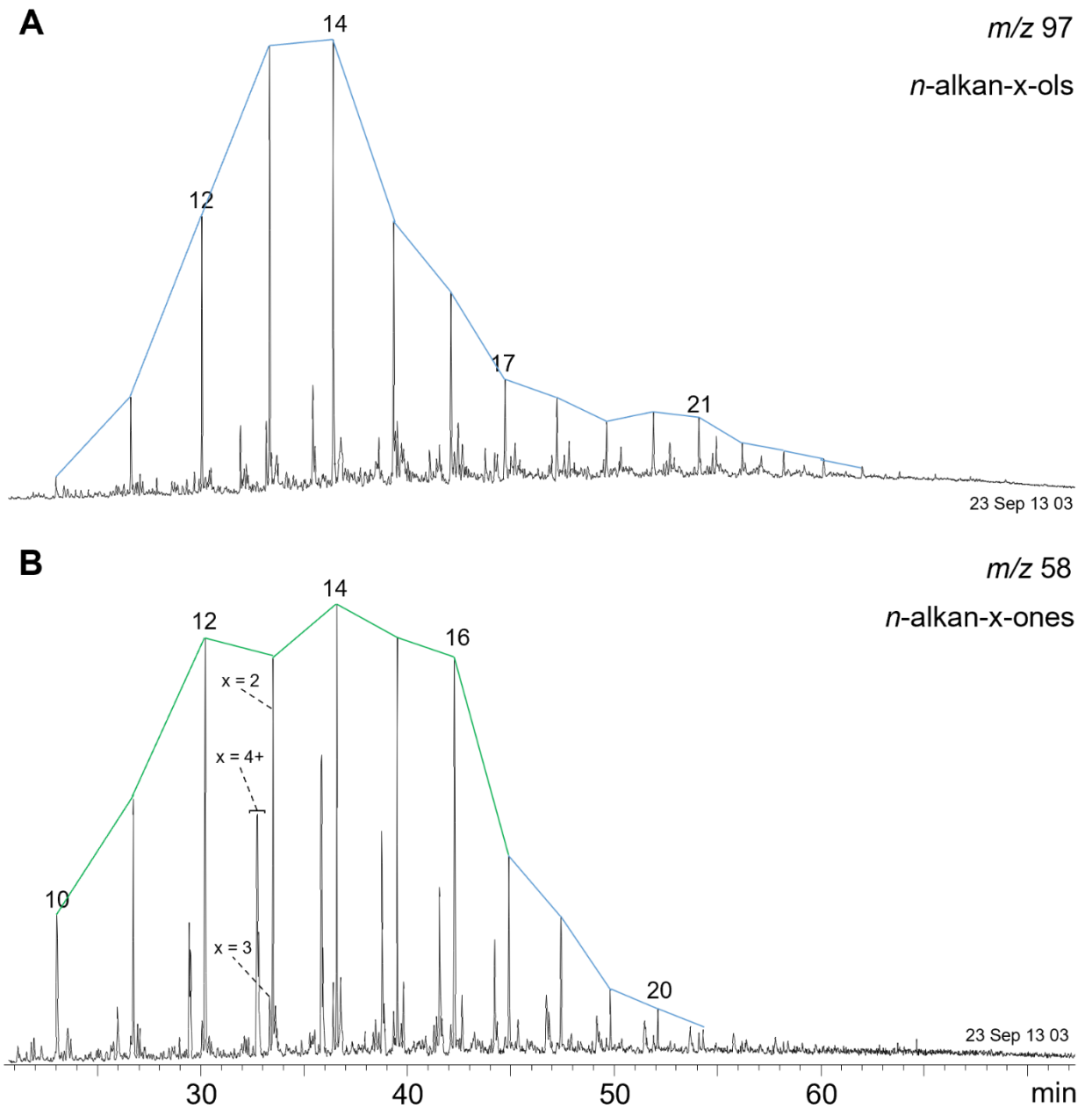


Fig. S14. Oxygen containing *n*-alkyl compounds in the pyrolysate of *S. nanum.* **a**, Partial *m/z* 97 mass chromatogram showing *n*-alcohols, i.e. x-hydroxyalkanes with one –OH moiety in position x, where x runs from position 2 to the middle of the alkyl chain. The positional isomers are largely coeluting. **b,** Partial *m/z* 58 mass chromatogram showing *n*-alkyl ketones. Compounds are identified by carbon number. Carbon number regions without carbon number preference are highlighted in blue and even-over-odd predominance in green. Alkanes are identified by carbon number.

Table S1. Biomarker ratios

	MPR[d]	R_c(MPR)[e]	Pr/Ph[f]	Pr/*n*-C_{17}[g]	Ph/*n*-C_{18}[h]	C_{max}[i]	OEP_{15-19}[j]	OEP_{23-27}[j]	OEP_{25-29}[j]
Matrix[a]	0.97	0.93%	3.1	0.71	0.27	15 & 25	1.09	1.43	1.56
Fossil[b]	0.90	0.90%	4.7	0.61	0.21	15	1.16	1.56	1.54
Pyrolysate[c]	0.93	0.92%	n.d.[k]	0.0	0.0	14	0.88	1.03	1.08

(a) Sample 23B200, the rock matrix surrounding *Spongiophyton* fossils.
(b) Solvent extract of isolated *Spongiophyton* (sample 23B201).
(c) Microdistillation pyrolysate (500°C, 10 min) on isolated and pre-extracted *Spongiophyton* (sample 23B201).
(d) Methylphenanthrene Ratio MPR = 2-MP/1-MP integrated in *m/z* 191; MP = methylphenanthrene.
(e) Computed vitrinite reflectance equivalent R_c = 1.1*log(MPR)+0.95 (ref(*131*)).
(f) Pr = pristane, Ph = phytane integrated in *m/z* 85 and corrected to correspond to integration in full scan (correction factor 1.058).
(g) Integrated in *m/z* 85 and corrected to correspond to integration in full scan (correction factor = 1.55).
(h) Integrated in *m/z* 85 and corrected to correspond to integration in full scan (correction factor = 1.49).
(i) Carbon number of highest concentrated *n*-alkane in chromatogram. Two values indicate bimodal distribution.
(j) Odd over Even Preference of *n*-alkanes in the given carbon number range. $OEP_{n-m} = (C_n + 6C_{n+2} + C_{n+4})/(4C_{n+1} + 4C_{n+3})$.
(k) n.d. = not detected.

	Steranes % chol:erg:stig[l]	MA Ster % chol:erg:stig[m]	TA Ster % chol:erg:stig[n]	TA MeSter % chol:erg:stig[o]	C_{27} 20R βαα/ααα[p]	C_{29} 20R βαα/ααα[q]	C_{29} ααα S/(S+R)[q]	C_{27} αββ/(ααα+αββ)[p]	C_{29} αββ/(ααα+αββ)[q]
Matrix	25:19:56	26:27:47	26:26:48	20:34:46	0.25	0.25	20%	13%	16%
Fossil	41:26:34	40:30:31	38:29:33	26:42:32	0.27	0.38	13%	17%	23%
Pyrolysate	29:23:48	33:34:33	n.d.	n.d.	0.39	1.1	n.d.	19%	n.d.

(l) Percentages of saturated steranes cholestane (chol), ergostane (erg) and stigmastane (stig) measured in MRM $M^{+\cdot} \rightarrow 217$ precursor-product transitions. Included isomers: diasteranes βα-20S+R, regular steranes ααα-20S+R, αββ-20S+R and βαα-20R. ααα = 5α(H),14α(H),17α(H); αββ = 5α(H),14β(H),17β(H); βαα = 5β(H),14α(H),17αβ(H).
(m) Percentages of monoaromatic (MA) steroids (Ster) including cholesteroids (chol), ergosteroids (erg) and stigmasteroids (stig) measured in *m/z* 253 selected ion chromatograms. Included are S and R isomers of structures I, II, V and VII following the nomenclature of ref(*132*).
(n) Percentages of triaromatic (TA) steroids measured in *m/z* 231 selected ion chromatograms including S and R isomers.
(o) Percentages of A-ring methylated triaromatic steroids (TA MeSter) measured in *m/z* 245 selected ion chromatograms including S and R isomers of 2-, 3- and 4-methyl chol, erg and stig.
(p) Cholestane isomer ratio (see footnote l).
(q) Stigmastane isomer ratio (see footnote l).

	Chol dia/reg[r]	Erg dia/reg[r]	Stig dia/reg[r]	C_{27} Hop Ts/(Ts+Tm)[s]	C_{30} Hop βα/(βα+αβ)[t]	C_{31} Hop S/(S+R)[u]	C_{27}/C_{30} Hop[v]	C_{29}/C_{30} Hop[w]	C_{31}/C_{30} Hop[x]
Matrix	0.41	0.33	0.32	33%	14%	55%	0.62	1.0	0.96
Fossil	0.46	0.43	0.33	29%	17%	49%	2.0	1.5	1.1
Pyrolysate	0.00	0.00	0.00	6.1%	27%	48%	1.6	1.3	1.8

(r) Diasterane/regular sterane ratios of cholestane, ergostane and stigmastane. Included isomers as defined in footnote l.
(s) Ts = 18α(H)-22,29,30-trisnorneohopane, Tm = 17α(H)-22,29,30-trisnorhopane.
(t) βα = 17β(H),21α(H)-hopane (moretane), αβ = 17α(H),21β(H)-hopane.
(u) S and R = 22S and 22R 17α(H),21β(H)-homohopane.
(v) C_{27}/C_{30} Hop = (Ts + Tm + 17β(H)-trisnorhopane) / (αβ + βα-hopane).
(w) C_{29}/C_{30} Hop = (C_{29} αβ-30-norhopane) / (C_{30} αβ-hopane).
(x) C_{31}/C_{30} Hop = (C_{31} 22S+R αβ-homohopane) / (C_{30} αβ-hopane).

	HHI[y]	2-MHI[z]	3-MHI[aa]	GI[bb]	Ster/Hop[cc]				
Matrix	2.8%	1.5%	1.0%	2.8%	0.30				
Fossil	n.d.	n.d.	n.d.	3.9%	0.28				
Pyrolysate	1.7%	n.d.	0.9%	1.8%	0.03				

(y) Homohopane Index HHI = (C_{35} 22S+R αβ-pentakishomohopane)/Σ(C_{31} to C_{35} 22S+R αβ-homohopanes).
(z) 2-Methylhopane Index 2-MHI = (C_{31} αβ 2α+β-methylhopane) / (C_{30} αβ-hopane).
(aa) 3-Methylhopane Index 3-MHI = (C_{31} αβ 3β-methylhopane) / (C_{30} αβ-hopane).
(bb) Gammacerane Index GI = gammacerane / (gammacerane + αβ + βα C_{30} hopane).
(cc) Sterane/Hopane ratio Ster/Hop = Σ(C_{27} to C_{29} βα-diasteranes + 20R βαα + 20S+R ααα + 20S+R αββ regular steranes) / ((C_{27} Ts + Tm + β) + (C_{29} + C_{30} αβ + βα) + Σ (C_{31} to C_{35} 22S+R αβ + βα) hopanes).

Data S1. **Morphological measurements and results from multiple chemical analyses**. The spreadsheet contains separate sheets for data obtained via ToF-SIMS, LA-ICP-MS, elemental analysis, XPS, Rock-Eval pyrolysis, ^{13}C NMR spectroscopy, FTIR spectroscopy, and nitrogen isotope measurements.

REFERENCES AND NOTES

1. P. K. Strother, T. Servais, M. Vecoli, The effects of terrestrialization on marine ecosystems: The fall of CO_2. *Geol. Soc. Lond. Spec. Publ.* **339**, 37–48 (2010).

2. D. Edwards, L. Cherns, J. A. Raven, Could land-based early photosynthesizing ecosystems have bioengineered the planet in mid-Palaeozoic times? *Palaeontology* **58**, 803–837 (2015).

3. C. V. Rubinstein, P. Gerrienne, G. S. de la Puente, R. A. Astini, P. Steemans, Early Middle Ordovician evidence for land plants in Argentina (eastern Gondwana). *New Phytol.* **188**, 365–369 (2010).

4. G. Spaak, D. S. Edwards, C. B. Foster, A. Pagès, R. E. Summons, N. Sherwood, K. Grice, Environmental conditions and microbial community structure during the Great Ordovician Biodiversification Event; a multi-disciplinary study from the Canning Basin, Western Australia. *Glob. Planet. Change* **159**, 93–112 (2017).

5. M. Libertín, J. Kvaček, J. Bek, V. Žárský, P. Štorch, Sporophytes of polysporangiate land plants from the early Silurian period may have been photosynthetically autonomous. *Nat Plants* **4**, 269–271 (2018).

6. M. P. Nelsen, R. Lücking, C. K. Boyce, H. T. Lumbsch, R. H. Ree, No support for the emergence of lichens prior to the evolution of vascular plants. *Geobiology* **18**, 3–13 (2020).

7. R. Lücking, M. P. Nelsen, "Ediacarans, protolichens, and lichen-derived *Penicillium*," in *Transformative Paleobotany* (Elsevier, 2018), pp. 551–590; http://dx.doi.org/10.1016/B978-0-12-813012-4.00023-1.

8. R. Honegger, "Lichens and their allies past and present," in *Plant Relationships*, B. Scott, C. Mesarich, Eds. (The Mycota, 2023), pp. 133–183; https://link.springer.com/10.1007/978-3-031-16503-0_6.

9. W. E. Stein, G. D. Harmon, F. M. Hueber, *Spongiophyton* from the Lower Devonian of North America reinterpreted as a lichen. *Am. J. Bot.* **80**, 93 (1993).

10. A. H. Jahren, S. Porter, J. J. Kuglitsch, Lichen metabolism identified in Early Devonian terrestrial organisms. *Geology* **31**, 99–102 (2003).

11. W. A. Taylor, C. Free, C. Boyce, R. Helgemo, J. Ochoada, SEM analysis of *Spongiophyton* interpreted as a fossil lichen. *Int. J. Plant Sci.* **165**, 875–881 (2004).

12. R. Kräusel, "*Spongiophyton* nov. gen. (Tallophita) und *Haplostigma* Seward (Pteridophyta) im UnterDevon von Parana," in *Paleontologia Do Paraná: Volume Comemorativo Do 1.° Centenário Do Estado Do Paraná*, F. Lange, Ed. (Comissão de Comemorações do Centenário do Paraná, Paraná,1954), pp. 195–210.

13. P. G. Gensel, W. G. Chaloner, W. H. Forbes, *Spongiophyton* from the late Lower Devonian of New Brunswick and Quebec, Canada. *Palaeontology* **34**, 149–168 (1991).

14. B. J. Fletcher, D. J. Beerling, W. G. Chaloner, Stable carbon isotopes and the metabolism of the terrestrial Devonian organism *Spongiophyton*. *Geobiology* **2**, 107–119 (2004).

15. G. Gaia, V. R. Ribeiro, R. P. Ghilardi, F. N. Sousa, M. P. Llopart, F. Ricardi-Branco, Chemical and elementary characterization of *Spongiophyton nanum*: Understanding the phylogeny, paleoenvironment, and fossilization processes of an enigmatic flora. *Rev. Palaeobot. Palynol.* **316**, 104943 (2023).

16. M. E. Hale, Pseudocyphellae and pored epicortex in the parmeliaceae: Their delimitation and evolutionary significance. *Lichenologist* **13**, 1–10 (1981).

17. C. A. Zanetti, S. B. Barbosa, S. A. Adachi, M. P. Marcelli, Pseudocyphellae ontogeny and thallus anatomy in species of *Punctelia* Krog (Parmeliaceae, lichenized Ascomycota). *Acta Bot. Bras.* **31**, 51–57 (2017).

18. A. M. F. Tomescu, R. W. Tate, N. G. Mack, V. J. Calder, "Simulating fossilization to resolve the taxonomic affinities of thalloid fossils in Early Silurian (ca. 425 Ma) terrestrial assemblages," in *Biology of Lichens: Symbiosis, Ecology, Environmental Monitoring, Systematics, Cyber Applications*, T. Nash III, Ed. (Cambridge Univ. Press, 2010), pp. 183–190.

19. R. Honegger, “Fossil lichens from the Lower Devonian and their bacterial and fungal epi-and endobionts,” in *Biodiversity and Ecology of Fungi, Lichens, and Mosses* (Austrian Academy of Sciences, 2018), pp. 547–564.

20. E. Kushnir, A. Tietz, M. Galun, “Oil hyphae” of endolithic lichens and their fatty acid composition. *Protoplasma* **97**, 47–60 (1978).

21. W. B. Sanders, C. Ascaso, J. Wierzchos, Physical interactions of two rhizomorph-forming lichens with their rock substrate. *Bot. Acta* **107**, 432–439 (1994).

22. V. Veselá, V. Malavasi, P. Škaloud, A synopsis of green-algal lichen symbionts with an emphasis on their free-living lifestyle. *Phycologia* **63**, 317–338 (2024).

23. J. W. Bjerke, Revision of the lichen genus *Menegazzia* in Japan, including two new species. *Lichenologist* **36**, 15–25 (2004).

24. E. S. Hansen, B. Mccune, The lichen genus *Hypogymnia* in Greenland. *Folia Cryptogam. Est.* **47**, 13–20 (2010).

25. C. Ascaso, Lichens on rock substrates: Observation of the biomineralization processes. *Bibl. Lichenol.* **75**, 127–135 (2000).

26. C. Ascaso, L. G. Sancho, C. Rodriguez-Pascual, The weathering action of saxicolous lichens in maritime Antarctica. *Polar Biol.* **11**, 33–39 (1990).

27. J. A. Erdman, L. P. Gough, R. W. White, Calcium Oxalate as source of high ash yields in the terricolous lichen *Parmelia chlorochroa*. *Bryologist* **80**, 334 (1977).

28. O. V. Frank-Kamenetskaya, G. Y. Ivanyuk, M. S. Zelenskaya, A. R. Izatulina, A. O. Kalashnikov, D. Y. Vlasov, E. I. Polyanskaya, Calcium oxalates in lichens on surface of apatite-nepheline ore (Kola Peninsula, Russia). *Minerals* **9**, 656 (2019).

29. V. Souza-Egipsy, J. Wierzchos, J. V. García-Ramos, C. Ascaso, Chemical and ultrastructural features of the lichen-volcanic/sedimentary rock interface in a semiarid region (Almería, Spain). *Lichenologist* **34**, 155–167 (2002).

30. E. J. Baran, P. V. Monje, “Oxalate biominerals,” in *Biomineralization* (Wiley, 2008); vol. 4, pp. 219–254; https://onlinelibrary.wiley.com/doi/10.1002/9780470986325.ch7.

31. P. Modenesi, M. Piana, D. Pinna, Surface features in *Parmelia sulcata* (Lichenes) thalli growing in shaded or exposed habitats. *Nova Hedwigia* **66**, 535–547 (1998).

32. R. M. Silverstein, F. X. Webster, D. J. Kiemle, D. L. Bryce, *Spectrometric Identification of Organic Compounds* (John Wiley & Sons Ltd., ed. 8, 2014); www.wiley.com/en-us/Spectrometric+Identification+of+Organic+Compounds%2C+8th+Edition-p-9780470616376.

33. B. P. Tissot, D. H. Welte, *Petroleum Formation and Occurrence* (Springer, 1984); http://link.springer.com/10.1007/978-3-642-87813-8.

34. M. A. Lafuente Diaz, G. M. Del Fueyo, J. A. D’Angelo, M. A. Carrizo, How much does Chemotaxonomy help to resolve the overrepresented *Cycadolepis* Saporta (Bennettitales)? A case study of the Cretaceous of Patagonia, Argentina. *Rev. Palaeobot. Palynol.* **293**, 104489 (2021).

35. G. D. Abbott, I. W. Fletcher, S. Tardio, E. Hack, Exploring the geochemical distribution of organic carbon in early land plants: A novel approach. *Philos. Trans. R. Soc. B Biol. Sci.* **373**, 20160499 (2018).

36. S. R. Kelemen, M. Afeworki, M. L. Gorbaty, M. Sansone, P. J. Kwiatek, C. C. Walters, H. Freund, M. Siskin, A. E. Bence, D. J. Curry, M. Solum, R. J. Pugmire, M. Vandenbroucke, M. Leblond, F. Behar, Direct characterization of kerogen by X-ray and solid-state ^{13}C nuclear magnetic resonance methods. *Energy Fuels* **21**, 1548–1561 (2007).

37. P. Le Pogam, B. Legouin, A. Geairon, H. Rogniaux, F. Lohézic-Le Dévéhat, W. Obermayer, J. Boustie, A. C. Le Lamer, Spatial mapping of lichen specialized metabolites using LDI-MSI: Chemical ecology issues for *Ophioparma ventosa*. *Sci. Rep.* **6**, 37807 (2016).

38. H. I. Petersen, P. Rosenberg, H. P. Nytoft, Oxygen groups in coals and alginite-rich kerogen revisited. *Int. J. Coal. Geol.* **74**, 93–113 (2008).

39. Y. Il Lee, H. S. Lim, H. Il Yoon, Carbon and nitrogen isotope composition of vegetation on King George Island, maritime Antarctic. *Polar Biol.* **32**, 1607–1615 (2009).

40. A. H. L. Huiskes, H. T. S. Boschker, D. Lud, T. C. W. Moerdijk-Poortvliet, Stable isotope ratios as a tool for assessing changes in carbon and nutrient sources in antarctic terrestrial ecosystems. *Plant Ecol.* **182**, 79–86 (2006).

41. P. Hietz, W. Wanek, R. Wania, N. M. Nadkarni, Nitrogen-15 natural abundance in a montane cloud forest canopy as an indicator of nitrogen cycling and epiphyte nutrition. *Oecologia* **131**, 350–355 (2002).

42. I. Bobrovskiy, S. W. Poulton, J. M. Hope, J. J. Brocks, Impact of aerobic reworking of biomass on steroid and hopanoid biomarker parameters recording ecological conditions and thermal maturity. *Geochim. Cosmochim. Acta* **364**, 114–128 (2024).

43. W. G. Chaloner, M. K. Mensah, M. D. Crane, Non-vascular land plants from the Devonian of Ghana. *Palaentology* **17**, 925–947 (1974).

44. H. Arnott, F. Pautard, "Calcification in plants," in *Biological Calcification*, H. Schraer, Ed. (Appleton-Century-Crofts, 1970), pp. 375–440.

45. R. Honegger, D. Edwards, L. Axe, The earliest records of internally stratified cyanobacterial and algal lichens from the Lower Devonian of the Welsh Borderland. *New Phytol.* **197**, 264–275 (2013).

46. T. N. Taylor, H. Hass, W. Remy, H. Kerp, The oldest fossil lichen. *Nature* **378**, 244–244 (1995).

47. I. V. Karatygin, N. S. Snigirevskaya, S. V. Vikulin, The most ancient terrestrial lichen *Winfrenatia reticulata*: A new find and new interpretation. *Paleontol. J.* **43**, 107–114 (2009).

48. D. Edwards, L. Axe, R. Honegger, Contributions to the diversity in cryptogamic covers in the mid-Palaeozoic: *Nematothallus* revisited. *Bot. J. Linn. Soc.* **173**, 505–534 (2013).

49. D. Edwards, R. Honegger, L. Axe, J. L. Morris, Anatomically preserved Silurian "nematophytes" from the Welsh Borderland (UK). *Bot. J. Linn. Soc.* **187**, 272–291 (2018).

50. Q. Yang, Y. Wang, R. Lücking, T. H. Lumbsch, Z. Du, Y. Chen, M. Bai, D. Ren, J. Wei, H. Li, Y. Wang, X. Wei, The Jurassic epiphytic macrolichen *Daohugouthallus* reveals the oldest lichen-plant interaction in a Mesozoic forest ecosystem. *iScience* **26**, 105770 (2023).

51. I. Kranner, R. Beckett, A. Hochman, T. H. Nash, Desiccation-tolerance in lichens: A review. *Bryologist* **111**, 576–593 (2008).

52. R. L. Mitchell, C. Strullu-Derrien, P. Kenrick, Biologically mediated weathering in modern cryptogamic ground covers and the early paleozoic fossil record. *J. Geol. Soc. London* **176**, 430–439 (2019).

53. P. Gerrienne, T. Servais, M. Vecoli, Plant evolution and terrestrialization during Palaeozoic times—The phylogenetic context. *Rev. Palaeobot. Palynol.* **227**, 4–18 (2016).

54. T. J. Algeo, S. E. Scheckler, Terrestrial-marine teleconnections in the Devonian: Links between the evolution of land plants, weathering processes, and marine anoxic events. *Philos. Trans. R. Soc. Lond. B Biol. Sci.* **353**, 113–130 (1998).

55. W. Elbert, B. Weber, S. Burrows, J. Steinkamp, B. Büdel, M. O. Andreae, U. Pöschl, Contribution of cryptogamic covers to the global cycles of carbon and nitrogen. *Nat. Geosci.* **5**, 459–462 (2012).

56. P. Porada, B. Weber, W. Elbert, U. Pöschl, A. Kleidon, Estimating impacts of lichens and bryophytes on global biogeochemical cycles. *Global Biogeochem. Cycles* **28**, 71–85 (2014).

57. N. L. Archilha, G. R. Costa, G. R. B. Ferreira, G. B. Z. L. Moreno, A. S. Rocha, B. C. Meyer, A. C. Pinto, E. X. S. Miqueles, M. B. Cardoso, H. Westfahl Jr., MOGNO, the nano and microtomography beamline at Sirius, the Brazilian synchrotron light source. *J. Phys. Conf. Ser.* **2380**, 012123 (2022).

58. ASTM D7708-14, Standard Test Method for Microscopical Determination of the Reflectance of Vitrinite Dispersed in Sedimentary Rocks (Advancing Standards Transforming Markets, 2014); https://store.astm.org/d7708-14.html.

59. E. L. Zodrow, J. A. D'Angelo, M. Mastalerz, C. J. Cleal, D. Keefe, Phytochemistry of the fossilized-cuticle frond *Macroneuropteris macrophylla* (Pennsylvanian seed fern, Canada). *Int. J. Coal Geol.* **84**, 71–82 (2010).

60. J. A. D'Angelo, E. L. Zodrow, M. Mastalerz, Compression map, functional groups and fossilization: A chemometric approach (Pennsylvanian neuropteroid foliage, Canada). *Int. J. Coal Geol.* **90–91**, 149–155 (2012).

61. J. A. D'Angelo, L. B. Escudero, W. Volkheimer, E. L. Zodrow, Chemometric analysis of functional groups in fossil remains of the *Dicroidium* flora (Cacheuta, Mendoza, Argentina): Implications for kerogen formation. *Int. J. Coal Geol.* **87**, 97–111 (2011).

62. J. A. D'Angelo, E. L. Zodrow, Fossil cutin of *Johnstonia coriacea* (Corystospermaceae, Upper Triassic, Cacheuta, Argentina). *Int. J. Coal Geol.* **189**, 70–74 (2018).

63. M. A. Lafuente Diaz, J. A. D'angelo, G. M. Del Fueyo, E. L. Zodrow, Fossilization model for *Squamastrobus tigrensis* foliage in a volcanic-ash deposit: Implications for preservation and taphonomy (Podocarpaceae, Lower Cretaceous, Argentina). *Palaios* **33**, 323–337 (2018).

64. M. A. Lafuente Diaz, J. A. D'Angelo, G. M. Del Fueyo, M. A. Carrizo, FTIR spectroscopic features of the pteridosperm *Ruflorinia orlandoi* and host rock (Springhill Formation, Lower Cretaceous, Argentina). *J. South Am. Earth Sci.* **99**, 102520 (2020).

65. H. C. N. Tolentino, M. M. Soares, C. A. Perez, F. C. Vicentin, D. B. Abdala, D. Galante, V. D. C. Teixeira, D. H. C. de Araújo, H. Westfahl, CARNAÚBA: The coherent x-ray nanoprobe beamline for the brazilian synchrotron SIRIUS/LNLS. *J. Phys. Conf. Ser.* **849**, 012057 (2017).

66. V. A. Solé, E. Papillon, M. Cotte, P. Walter, J. Susini, A multiplatform code for the analysis of energy-dispersive X-ray f luorescence spectra. *Spectrochim. Acta B At. Spectrosc.* **62**, 63–68 (2007).

67. Q. Wang, Q. Liu, Z. Wang, H. Liu, J. Bai, X-ray photoelectron spectroscopy investigation of nitrogen transformation in Chinese oil shales during pyrolysis. *Oil Shale* **34**, 129–145 (2017).

68. B. C. Meyer, T. C. R. Rocha, S. A. L. Luiz, A. Clarindo Pinto, H. Westfahl, "Simulation and optimization of the Sirius IPE soft x-ray beamline," in *Advances in Computational Methods for X-Ray Optics IV*, K. Sawhney, O. Chubar, Eds. (SPIE, 2017), vol. 10388, p. 13.

69. B. Ravel, M. Newville, ATHENA, ARTEMIS, HEPHAESTUS: Data analysis for X-ray absorption spectroscopy using IFEFFIT. *J. Synchrotron Radiat.* **12**, 537–541 (2005).

70. B. W. Johnson, C. Mettam, S. W. Poulton, Combining nitrogen isotopes and redox proxies strengthens paleoenvironmental interpretations: Examples from neoproterozoic snowball Earth sediments. *Front. Earth Sci.* **10**, 745830 (2022).

71. M. A. Kipp, E. E. Stüeken, C. A. E. Strömberg, W. H. Brightly, V. M. Arbour, B. Erdei, R. S. Hill, K. R. Johnson, J. Kvaček, J. C. McElwain, I. M. Miller, M. Slodownik, V. Vajda, R. Buick, Nitrogen isotopes reveal independent origins of N_2-fixing symbiosis in extant cycad lineages. *Nat. Ecol. Evol.* **8**, 57–69 (2024).

72. T. B. Coplen, W. A. Brand, M. Gehre, M. Gröning, H. A. J. Meijer, B. Toman, R. M. Verkouteren, New guidelines for δ 13 C measurements. *Anal. Chem.* **78**, 2439–2441 (2006).

73. F. Meneau, A. R. Passos, P. R. A. F. Garcia, P. Vinaches, L. B. Manoel, T. A. Kalile, J. P. Zerba, G. L. M. P. Rodrigues, E. Miqueles, G. Baraldi, J. Polli, B. C. Meyer, S. A. L. Luiz, C. Polo, Cateretê: The coherent X-ray scattering beamline at the fourth-generation synchrotron facility SIRIUS. *Acta Crystallogr. A Found. Adv.* **77**, C283–C283 (2021).

74. L. Liu, N. Milas, A. H. C. Mukai, X. R. Resende, F. H. De Sá, The sirius project. *J. Synchrotron Radiat.* **21**, 904–911 (2014).

75. C. Paton, J. Hellstrom, B. Paul, J. Woodhead, J. Hergt, Iolite: Freeware for the visualisation and processing of mass spectrometric data. *J. Anal. At. Spectrom* **26**, 2508–2518 (2011).

76. J. A. Petrus, D. M. Chew, M. I. Leybourne, B. S. Kamber, A new approach to laser-ablation inductively-coupled-plasma mass-spectrometry (LA-ICP-MS) using the flexible map interrogation tool 'Monocle'. *Chem. Geol.* **463**, 76–93 (2017).

77. B. Paul, J. Petrus, D. Savard, J. Woodhead, J. Hergt, A. Greig, C. Paton, P. Rayner, Time resolved trace element calibration strategies for LA-ICP-MS. *J. Anal. At. Spectrom* **38**, 1995–2006 (2023).

78. M. Guillong, K. Hametner, E. Reusser, S. A. Wilson, D. Günther, Preliminary characterisation of new glass reference materials (GSA-1G, GSC-1G, GSD-1G and GSE-1G) by laser ablation-inductively coupled plasma-mass spectrometry using 193 nm, 213 nm and 266 nm wavelengths. *Geostand. Geoanal. Res.* **29**, 315–331 (2005).

79. K. P. Jochum, U. Nohl, K. Herwig, E. Lammel, B. Stoll, A. W. Hofmann, GeoReM: A new geochemical database for reference materials and isotopic standards. *Geostand. Geoanal. Res.* **29**, 333–338 (2005).

80. E. Lafargue, F. Marquis, D. Pillot, Rock-Eval 6 applications in hydrocarbon exploration, production, and soil contamination studies. *Rev. Inst. Fr. Pét.* **53**, 421–437 (1998).

81. J. J. Brocks, Millimeter-scale concentration gradients of hydrocarbons in Archean shales: Live-oil escape or fingerprint of contamination? *Geochim. Cosmochim. Acta* **75**, 3196–3213 (2011).

82. J. J. Brocks, E. Grosjean, G. A. Logan, Assessing biomarker syngeneity using branched alkanes with quaternary carbon (BAQCs) and other plastic contaminants. *Geochim. Cosmochim. Acta* **72**, 871–888 (2008).

83. J. J. Brocks, J. M. Hope, Tailing of chromatographic peaks in GC-MS caused by interaction of halogenated solvents with the ion source. *J. Chromatogr. Sci.* **52**, 471–475 (2014).

84. A. S. Merdith, S. E. Williams, A. S. Collins, M. G. Tetley, J. A. Mulder, M. L. Blades, A. Young, S. E. Armistead, J. Cannon, S. Zahirovic, R. D. Müller, Extending full-plate tectonic models into deep time: Linking the neoproterozoic and the phanerozoic. *Earth Sci. Rev.* **214**, 103477 (2021).

85. E. Pereira, "Evolução tectono-sedimentar do intervalo Ordoviciano-Devoniano da Bacia do Paraná," thesis, Universidade de São Paulo (2000).

86. B. Becker-Kerber, G. L. Osés, J. F. Curado, M. De Almeida Rizzutto, I. D. Rudnitzki, G. R. Romero, S. Y. Onary-Alves, V. G. Benini, D. Galante, F. Rodrigues, P. V. Buck, E. C. Rangel, R. P. Ghilardi, M. L. A. F. Pacheco, Geobiological and diagenetic insights from Malvinokaffric Devonian biota (Chapada group, Paraná Basin, Brazil): Paleobiological and paleoenvironmental implications. *Palaios* **32**, 238–249 (2017).

87. J. H. G. Melo, "The malvinokaffric realm in the devonian of Brazil," in *Devonian of the World: Proceedings of the 2nd International Symposium on the Devonian System*, N. J. McMillam, A. F. Embry, D. J. Glass, Eds. (Canadian Society of Petroleum Geologists, 1988), vol. 14, pp. 669–703.

88. Y. Grahn, P. M. Mauller, E. Pereira, S. Loboziak, Palynostratigraphy of the Chapada Group and its significance in the Devonian stratigraphy of the Paraná Basin, south Brazil. *J. South Am. Earth Sci.* **29**, 354–370 (2010).

89. Y. Grahn, E. Pereira, S. Bergamaschi, Silurian and lower Devonian chitinozoan biostratigraphy of the Paraná Basin in Brazil and Paraguay. *Palynology* **24**, 147–176 (2000).

90. D. Sedorko, R. G. Netto, S. M. Scheffler, R. S. Horodyski, E. P. Bosetti, R. P. Ghilardi, P. M. Mauller, M. R. de Vargas, R. Videira-Santos, R. C. da Silva, L. Myzynski-Junior, Paleoecologic trends of Devonian Malvinokaffric fauna from the Paraná Basin as evidenced by trace fossils. *J. South Am. Earth Sci.* **109**, 103200 (2021).

91. R. Kräusel, B. Venkatachala, Devonische Spongiophytaceen aus Ost- und West-Asien. *Senck. Lethaea* **47**, 215–251 (1966).

92. F. M. Michel, J. MacDonald, J. Feng, B. L. Phillips, L. Ehm, C. Tarabrella, J. B. Parise, R. J. Reeder, Structural characteristics of synthetic amorphous calcium carbonate. *Chem. Mater.* **20**, 4720–4728 (2008).

93. M. Bačkor, S. Loppi, Interactions of lichens with heavy metals. *Biol. Plant.* **53**, 214–222 (2009).

94. V. Krajanová, Discoveries and identification methods of metal oxalates in lichens and their mineral associations: A review of past studies and analytical options for lichenologists. *Fungal Biol. Rev.* **43**, 100287 (2023).

95. M. Malekhosseini, H. J. Ensikat, V. E. McCoy, T. Wappler, M. Weigend, L. Kunzmann, J. Rust, Traces of calcium oxalate biomineralization in fossil leaves from late Oligocene maar deposits from Germany. *Sci. Rep.* **12**, 15959 (2022).

96. M. T. Suekuni, P. R. Craddock, J. T. Douglas, A. E. Pomerantz, A. M. Allgeier, Critical practices for the preparation and analysis of Kerogen. *Energy Fuels* **36**, 8828–8843 (2022).

97. X. H. Guan, Y. Liu, D. Wang, Q. Wang, M. S. Chi, S. Liu, C. G. Liu, Three-dimensional structure of a Huadian oil shale Kerogen model: An experimental and theoretical study. *Energy Fuels* **29**, 4122–4136 (2015).

98. M. N. Siddiqui, M. F. Ali, J. Shirokoff, Use of X-ray diffraction in assessing the aging pattern of asphalt fractions. *Fuel* **81**, 51–58 (2002).

99. A. M. Orendt, I. S. O. Pimienta, S. R. Badu, M. S. Solum, R. J. Pugmire, J. C. Facelli, D. R. Locke, K. W. Chapman, P. J. Chupas, R. E. Winans, Three-dimensional structure of the siskin green river oil shale kerogen model: A comparison between calculated and observed properties. *Energy Fuels* **27**, 702–710 (2013).

100. P. Leinweber, J. Kruse, F. L. Walley, A. Gillespie, K. U. Eckhardt, R. I. R. Blyth, T. Regier, Nitrogen *K*-edge XANES – An overview of reference compounds used to identify "unknown" organic nitrogen in environmental samples. *J. Synchrotron Radiat.* **14**, 500–511 (2007).

101. Y. Zubavichus, M. Zharnikov, A. Shaporenko, O. Fuchs, L. Weinhardt, C. Heske, E. Umbach, J. D. Denlinger, M. Grunze, Soft X-ray induced decomposition of phenylalanine and tyrosine: A comparative study. *Chem. A Eur. J.* **108**, 4557–4565 (2004).

102. G. D. Cody, H. Ade, C. M. O. D. Alexander, T. Araki, A. Butterworth, H. Fleckenstein, G. Flynn, M. K. Gilles, C. Jacobsen, A. L. D. Kilcoyne, K. Messenger, S. A. Sandford, T. Tyliszczak, A. J. Westphal, S. Wirick, H. Yabuta, Quantitative organic and light-element analysis of comet 81P/Wild 2 particles using C-, N-, and O-μ-XANES. *Meteorit. Planet. Sci.* **43**, 353–365 (2008).

103. S. R. Kelemen, M. L. Gorbaty, P. J. Kwiatek, Quantification of nitrogen forms in argonne premium coals. *Energy Fuels* **8**, 896–906 (1994).

104. W. M. K. Matsumura, M. Di Pasquo, R. Iannuzzi, E. P. Bosetti, "Plant diversification through the Devonian in Brazil," in *Brazilian Paleofloras: From Paleozoic to Holocene* (Springer Nature, 2024), pp. 1–79.

105. D. Sedorko, E. P. Bosetti, R. P. Ghilardi, L. José, M. Júnior, R. C. Silva, S. M. Scheffler, Paleoenvironments of a regressive Devonian section from Paraná Basin (Mato Grosso do Sul state) by integration of ichnologic, taphonomic and sedimentologic analyses. *Braz. J. Geol.* **48**, 805–820 (2018).

106. N. N. da Silva, I. M. Abreu, J. R. Cerqueira, D. N. do Amaral, K. S. Garcia, L. T. S. Santos, O. M. C. Oliveira, A. F. de S. Queiroz, M. E. Machado, Paleoenvironmental characterization of the Ponta Grossa formation (Devonian) at the northwest border of the Paraná Basin, Brazil. *J. South Am. Earth Sci.* **130**, 104540 (2023).

107. I. Bobrovskiy, J. M. Hope, A. Krasnova, A. Ivantsov, J. J. Brocks, Molecular fossils from organically preserved Ediacara biota reveal cyanobacterial origin for *Beltanelliformis*. *Nat. Ecol. Evol.* **2**, 437–440 (2018).

108. M. A. Ikeda, H. Nakamura, K. Sawada, Organic Geochemistry Aliphatic hydrocarbons in the lichen class Lecanoromycetes and their potential use as chemotaxonomic indicators and biomarkers. *Org. Geochem.* **179**, 104588 (2023).

109. G. D. Love, C. E. Snape, A. D. Carr, R. C. Houghton, Release of covalently-bound alkane biomarkers in high yields from kerogen via catalytic hydropyrolysis. *Org. Geochem.* **23**, 981–986 (1995).

110. G. Vinnichenko, A. J. M. Jarrett, J. M. Hope, J. J. Brocks, Discovery of the oldest known biomarkers provides evidence for phototrophic bacteria in the 1.73 Ga Wollogorang Formation, Australia. *Geobiology* **18**, 544–559 (2020).

111. V. M. Dembitsky, Lipids of lichens. *Prog. Lipid Res.* **31**, 373–397 (1992).

112. I. Bobrovskiy, A. Nagovitsyn, J. M. Hope, E. Luzhnaya, J. J. Brocks, Guts, gut contents, and feeding strategies of Ediacaran animals. *Curr. Biol.* **32**, 5382–5389.e3 (2022).

113. J. Brocks, I. Bobrovskiy, Some animals make plant sterols. *Science* **380**, 455–456 (2023).

114. I. Melendez, K. Grice, L. Schwark, Exceptional preservation of palaeozoic steroids in a diagenetic continuum. *Sci. Rep.* **3**, 2768 (2013).

115. B. A. Stankiewicz, D. E. G. Briggs, R. Michels, M. E. Collinson, M. B. Flannery, R. P. Evershed, Alternative origin of aliphatic polymer in kerogen. *Geology* **28**, 559–562 (2000).

116. K. J. Niklas, Chemical examinations of some non-vascular Paleozoic plants. *Brittonia* **28**, 113–137 (1976).

117. K. J. Niklas, W. G. Chaloner, Chemotaxonomy of some problematic palaeozoic plants. *Rev. Palaeobot. Palynol.* **22**, 81–104 (1976).

118. V. C. Farmer, *The Infrared Spectra of Minerals* (Mineralogical Society of Great Britain and Ireland, 1974); https://pubs.geoscienceworld.org/books/book/1871/.

119. J. D. Russell, A. R. Fraser, “Infrared methods,” in *Clay Mineralogy: Spectroscopic and Chemical Determinative Methods*, M. J. Wilson, Ed. (Springer, 1994), pp. 11–67; http://link.springer.com/10.1007/978-94-011-0727-3_2.

120. W. M. K. Matsumura, N. M. Balzaretti, R. Iannuzzi, Fourier transform infrared characterization of the Middle Devonian non-vascular plant *Spongiophyton*. *Palaeontology* **59**, 365–386 (2016).

121. H. Ganz, W. Kalkreuth, Application of infrared spectroscopy to the classification of kerogen types and the evaluation of source rock and oil shale potentials. *Fuel* **66**, 708–711 (1987).

122. D. Zdebska, On *Spongiophyton* from the Lower Devonian of Poland. *Acta Palaeobot.* **19**, 13–20 (1978).

123. G. Pacyna, M. Barbacka, Polish Palaeobotany: 750 Million years of plant history as revealed in a century of studies. Palaeozoic macrofossils. *Acta Soc. Bot. Pol.* **91**, 9123 (2022).

124. D. Edwards, Fragmentary non-vascular plant microfossils from the late Silurian of Wales. *Bot. J. Linn. Soc.* **84**, 223–256 (1982).

125. Y. Guo, D. Wang, Studies on plant cuticles from the Lower-Middle Devonian of China. *Rev. Palaeobot. Palynol.* **227**, 42–51 (2016).

126. E. M. Boureau, D. P. Pons, Sur des empreintes végétales dévoniennes du Sud de la Bolivie. *Comptes Rendus l'Académie des Sci.* **276**, 2151–2153 (1973).

127. A. D. Farjat, M. S. Riglos, J. L. Ortiz, Silurian and devonian heteroconchia cardiomorphi bivalves from Bolivia. *Ameghiniana* **58**, 385–400 (2021).

128. M. Di Pasquo, S. Noetinger, P. Isaacson, G. Grader, D. Starck, E. Morel, H. A. Folnagy, Mid-Late Devonian assemblages of herbaceous lycophytes from northern Argentina and Bolivia: Age assessment with palynomorphs and invertebrates and paleobiogeographic importance. *J. South Am. Earth Sci.* **63**, 70–83 (2015).

129. P. Gerrienne, M. Fairon-Demaret, J. Galtier, H. Lardeux, B. Meyer-Berthaud, S. Régnault, Plants associated with tentaculites in a New Early Devonian locality from Morocco. *Abh. Geol. Bundesanst.* **54**, 323–335 (1999).

130. W. M. K. Matsumura, R. Iannuzzi, Plantas devonianas do Brasil e seu significado bioestratigráfico. *Bol. Mus. Para. Emílio Goeldi, Ciênc. Nat.* **10**, 19–36 (2021).

131. M. Radke, Application of aromatic compounds as maturity indicators in source rocks and crude oils. *Mar. Pet. Geol.* **5**, 224–236 (1988).

132. K. E. Peters, C. C. Walters, J. M. Moldowan, *The Biomarker Guide* (Cambridge Univ. Press, 2004); www.cambridge.org/core/product/identifier/9781107326040/type/book.